Bioactive Materials 20 (2023) 404–417

Contents lists available at ScienceDirect

Bioactive Materials

journal homepage: www.keaipublishing.com/en/journals/bioactive-materials

Carrier-free nanoprodrug for p53-mutated tumor therapy via concurrent delivery of zinc-manganese dual ions and ROS

Jinping Wang [a,b], Chang Qu [e,f], Xinyue Shao [e], Guoqiang Song [e], Jingyu Sun [c], Donghong Shi [e,f], Ran Jia [e], Hailong An [a,**], Hongjun Wang [b,c,d,*]

[a] Key Laboratory of Molecular Biophysics of Hebei Province, Institute of Biophysics, School of Health Sciences and Biomedical Engineering, Hebei University of Technology, 300401, Tianjin, PR China
[b] Department of Biomedical Engineering, Stevens Institute of Technology, Hoboken, NJ, 07030, United States
[c] Department of Chemistry and Chemical Biology, Stevens Institute of Technology, Hoboken, NJ, 07030, United States
[d] Center for Healthcare Innovation, Stevens Institute of Technology, Hoboken, NJ, 07030, United States
[e] Key Laboratory of Molecular Biophysics of Hebei Province, Institute of Biophysics, School of Sciences, Hebei University of Technology, 300401, Tianjin, PR China
[f] State Key Laboratory of Reliability and Intelligence of Electrical Equipment, School of Electrical Engineering, Hebei University of Technology, Tianjin, 300130, PR China

ARTICLE INFO

Keywords:
p53-mutated tumor therapy
Wild-type p53 protein
Carrier-free nanoprodrug
Mn-ZnO_2 nanoparticle
Reactive oxygen species

ABSTRACT

Human cancers typically express a high level of tumor-promoting mutant p53 protein (Mutp53) with a minimal level of tumor-suppressing wild-type p53 protein (WTp53). In this regard, inducing Mutp53 degradation while activating WTp53 is a viable strategy for precise anti-tumor therapy. Herein, a new carrier-free nanoprodrug (*i.e.*, Mn-ZnO_2 nanoparticles) was developed for concurrent delivery of dual Zn-Mn ions and reactive oxygen species (ROS) within tumor to regulate the p53 protein for high anti-tumor efficacy. In response to the mild tumor acidic environment, the released Zn^{2+} and H_2O_2 from Mn-ZnO_2 NPs induced ubiquitination-mediated proteasomal degradation of Mutp53, while the liberative Mn^{2+} and increased ROS level activated the ATM-p53-Bax pathway to elevate WTp53 level. Both *in vitro* and *in vivo* results demonstrated that pH-responsive decomposition of Mn-ZnO_2 NPs could effectively elevate the intracellular dual Zn-Mn ions and ROS level and subsequently generate the cytotoxic hydroxyl radical (•OH) through the Fenton-like reaction. With the integration of multiple functions (*i.e.*, carrier-free ion and ROS delivery, tumor accumulation, p53 protein modulation, toxic •OH generation, and pH-activated MRI contrast) in a single nanosystem, Mn-ZnO_2 NPs demonstrate its superiority as a promising nanotherapeutics for p53-mutated tumor therapy.

1. Introduction

p53, a tumor suppressor protein, can regulate cancer cell death through transcriptional activation of multiple proapoptotic genes such as Bax [1–3]. However, in human cancers the level of wild-type p53 protein (WTp53) is rather low and in some cases even undetectable [4]. As a matter of fact, p53 mutation is oftentimes observed with more than 50% in most cancers, and up to 80% in those difficult-to-treat cancers such as high-grade serous ovarian cancers, triple-negative breast cancers, oesophageal cancers, small-cell lung cancers, and squamous cell lung cancers [5–7]. Typically, p53 mutation takes place in two distinct fashions [8]: 1) DNA contact mutation, *e.g.*, $p53^{R248Q}$ and $p53^{R273H}$, caused by directly binding DNA to the protein domains, 2) conformational mutation, *e.g.*, $p53^{R175H}$ and $p53^{H179R}$, caused by a full or partial distortion of the folding of DNA-binding domains. The mutant p53 proteins (Mutp53) not only completely lose the tumor-suppressive functions of the wild-type, but oftentimes acquire new inherent oncogenic functions, that is, a phenomenon termed as mutant p53 gain-of-function (GOF) [9,10]. Because of such a unique GOF, Mutp53 can actively promote tumor growth, invasiveness, and metastasis via regulation of the critical cellular processes from chromatin structure to metabolism [11–14]. To this end, elimination of Mutp53 while

Peer review under responsibility of KeAi Communications Co., Ltd.
* Corresponding author at: Department of Biomedical Engineering, Stevens Institute of Technology, Hoboken, NJ, 07030, United States.
** Corresponding author at: Key Laboratory of Molecular Biophysics of Hebei Province, Institute of Biophysics, School of Sciences, School of Health Sciences and Biomedical Engineering, Hebei University of Technology, 300401, Tianjin, PR China.
E-mail addresses: hailong_an@hebut.edu.cn (H. An), hongjun.wang@stevens.edu (H. Wang).

https://doi.org/10.1016/j.bioactmat.2022.06.005
Received 21 March 2022; Received in revised form 20 May 2022; Accepted 7 June 2022

increasing WTp53 is of great benefit in tumor therapy.

Given the high mutation rate of p53, Mutp53 becomes an attractive target in p53-mutated tumor therapy [15]. Among various strategies to reduce the Mutp53 level, the most straightforward one is through the proteasome or autophagy-induced degradation. For example, efforts have been made to degrade Mutp53 by virtue of small molecules such as NSC59984, Hsp90 inhibitor 17-AAG, and statins (*via* the proteasomal pathway) [16–18], or MCB-613, gambogic acid, and SAHA (*via* the autophagic pathway) [19–21]. Despite their efficiency in Mutp53 degradation, the identified challenges such as chemical toxicity and non-target effects motivate continuous endeavors to seek for more robust yet safer mechanisms to regulate p53 protein. Recently, Chen and co-workers reported that zinc ions (Zn^{2+}) could inhibit the mitochondrial electron transport chain (mETC) and promote the production of reactive oxygen species (ROS) (such as $O_2^{\cdot-}$ and H_2O_2) by increasing electron leakage to the oxygen at NADH-Q reductase (complex I) and ubiquinol-cytochrome-c reductase (complex III) of mETC [22]. More importantly, elevated intracellular Zn^{2+} level and endogenous ROS generation exhibit the capability of selectively degrading a panel of Mutp53 (both contact and conformational mutation), but not the WTp53, *via* the ubiquitination-mediated proteasomal (UPS) pathway [23]. Such observations partially prop our hypothesis that endogenous generation of ROS through Zn^{2+} in combination with exogenous supply of ROS would lead to more effective Mutp53 degradation.

Increasing evidence demonstrates that enhanced accumulation and stabilization of WTp53 could be achieved by activating the ataxia telangiectasia mutated (ATM)-p53 signaling pathway with a high concentration of manganese ions (Mn^{2+}) [24]. More specifically, Mn^{2+} exposure could cause the ATM activation *via* autophosphorylation and other established ATM phosphorylation targets (CHK2[T68] and H2AX [S139]), which subsequently induced the phosphorylation of p53 (serine 15). Thus, Mn^{2+} is actively involved in the ATM-regulated p53 phosphorylation [25] and the activated WTp53 then induce the transcription of proapoptotic Bax gene, responsible for tumor cell death or growth arrest [26]. Interestingly, ROS-induced ATM autophosphorylation on Ser1981 could also cause the phosphorylation of p53 on Ser15 [27]. Collectively, elevation of intracellular Mn^{2+}, Zn^{2+}, and ROS level could deliver an appealing strategy to activate WTp53 while simultaneously eliminating Mutp53 for cancer therapy. Furthermore, because of its Fenton catalytic activity, Mn^{2+} was also able to catalyze the formation of cytotoxic hydroxyl radical (•OH) from H_2O_2 and subsequently cause the apoptosis of cancer cells for effective eradication [28]. However, it remains highly challenging to selectively transport and retain exogeneous ROS and desirable metallic ions (*e.g.*, Zn^{2+} and Mn^{2+}) within targeted cells through the membranous ion channels and intracellular trafficking against the intrinsic efflux/storage processes [29]. Taking advantage of the unique competence of certain exotic materials such as long circulating polyethylene glycol [30] and high ion-binding hyperbranched polyglycerol [31], metallic compounds or ions of interest can be formulated into nanocomposites with these materials for better endocytosis. However, the rising concerns on undesirable immunoresponses from such synthetic materials [32] divert the efforts toward reduction or elimination of the use of exotic materials. In this regard, the preferred and compelling delivery system for dual ions and exogeneous ROS would be primarily composed of the stable formats of ions or ROS without the use of other materials. Ideally, such systems should maintain the structural integrity outside the cells and then exhibit the ability to manifestly elevate the intracellular dual Zn^{2+}-Mn^{2+} and ROS sufficient to respectively induce Mutp53 degradation while improving WTp53 level upon cellular uptake. Very recent study has demonstrated the capability of simultaneously delivering exogenous H_2O_2 and Zn^{2+} *via* pH-sensitive zinc peroxide nanoparticles (ZnO_2 NPs) [22]. Meanwhile, the similar ionic radius between Mn and Zn (0.66 Å and 0.60 Å, respectively) would allow to substitute the Zn^{2+} of the crystal lattice of ZnO_2 NPs with Mn^{2+} to yield the Mn-doped ZnO_2 nanosystem [33]. To this end, it is highly feasible to develop a multifunctional nanosystem, enabling simultaneous delivery of Mn-Zn dual ions and ROS suitable for p53-mutated tumor therapy.

In this study, ZnO_2 NPs doped with optimal Mn^{2+}, *i.e.*, Mn-ZnO_2 NPs were accordingly synthesized and used as a carrier-free nanoprodrug in order to selectively elevate intracellular Zn^{2+} and Mn^{2+} concentration while enhancing ROS formation (H_2O_2 and •OH) for Mutp53 degradation and WTp53 activation to achieve the synergistic cancer therapy (Scheme 1). The Mn-ZnO_2 NPs were stable under a neutral pH environment but completely decomposed to Mn^{2+}, Zn^{2+}, and H_2O_2 at the mild acidic circumstances. The physicochemical and biological properties of Mn-ZnO_2 NPs were comprehensively evaluated *in vitro* and *in vivo* with particular focuses on the release performance of Zn-Mn dual ions and ROS, •OH generation capacity, cellular uptake, Mutp53 degradation efficiency, WTp53 activation, and tumor therapeutic effect along with their tissue distribution and biosafety. Several unique attributes could be identified with the multifunctional Mn-ZnO_2 NPs including: 1) the rapid release of H_2O_2 and Zn^{2+} in an acidic microenvironment after cellular internalization to elevate endogenous ROS formation and induce Mutp53 degradation, 2) an increase of WTp53 *via* the ATM-p53-Bax pathway activated by the released Mn^{2+}, 3) the high biosafety and selectivity for bio-specific transport of metallic ions and ROS without exotic materials, 4) the *in vivo* magnetic resonance imaging (MRI) capabilities of Mn^{2+} for tracking tissue distribution of Mn-ZnO_2 NPs and guiding the therapeutic process, and 5) the generation of toxic •OH through the Fenton reaction of Mn^{2+} and H_2O_2 for enhanced antitumor efficiency. Along with successful demonstration of such carrier-free Mn-ZnO_2 NPs as a pH-sensitive prodrug to treat p53-mutated tumors, this study also provides blueprints to design other carrier-free nanosystems with varying ions and/or ROS delivery demands for cancer therapy.

2. Materials and methods

2.1. Materials

Zinc acetate ($Zn(OAc)_2$), polyvinylpyrrolidone (PVP, Mw = 360,000), hydrogen peroxide (H_2O_2, 30 wt% in H_2O), zinc chloride ($ZnCl_2$), sodium acetate, acetic acid, 2′,7′-dichlorofluorescin diacetate (DCFH-DA), ZnAF-2 DA, and calcein AM/propidium iodide (PI) staining kit were all purchased from Sigma-Aldrich (St. Louis, MO, USA). Manganese (II) chloride ($MnCl_2$), methylene blue (MB), Pierce™ quantitative peroxide (PQP) assay kit, and mitochondrial hydroxyl radical detection assay kit (MitoROS OH580) were purchased from Fisher Scientific (Waltham, MA, USA). All chemicals were used as received without further treatment.

2.2. Synthesis of ZnO_2 NPs

ZnO_2 NPs were fabricated following a simple and green wet chemistry approach with modification [22]. Briefly, 0.1 g of $Zn(OAc)_2$ and 0.1 g of PVP were dissolved in 5.0 mL of deionized (DI) water. Then, 0.5 mL of H_2O_2 was quickly added under a vigorous stirring. After reaction for 24 h, the unreacted residue was removed by centrifugation at 15,000 rpm for 15 min and rinsing three times with DI water. The final PVP-modified ZnO_2 NPs were re-dispersed in ethanol (95%) and used for the synthesis of Mn-ZnO_2 NPs.

2.3. Synthesis of Mn–ZnO_2 NPs

The Mn-doping was achieved using a cation-exchange approach. Specifically, 5 mL of the above-obtained ethanol solution of ZnO_2 NPs was mixed with 5 mL of $MnCl_2$ at different Mn concentrations and stirred at room temperature for 4 h. During the reaction, color of the solution gradually changed from milky white into yellowish-brown. Upon washing/centrifugation (15,000 rpm, 15 min), the resulting Mn-ZnO_2 NPs were collected for further use.

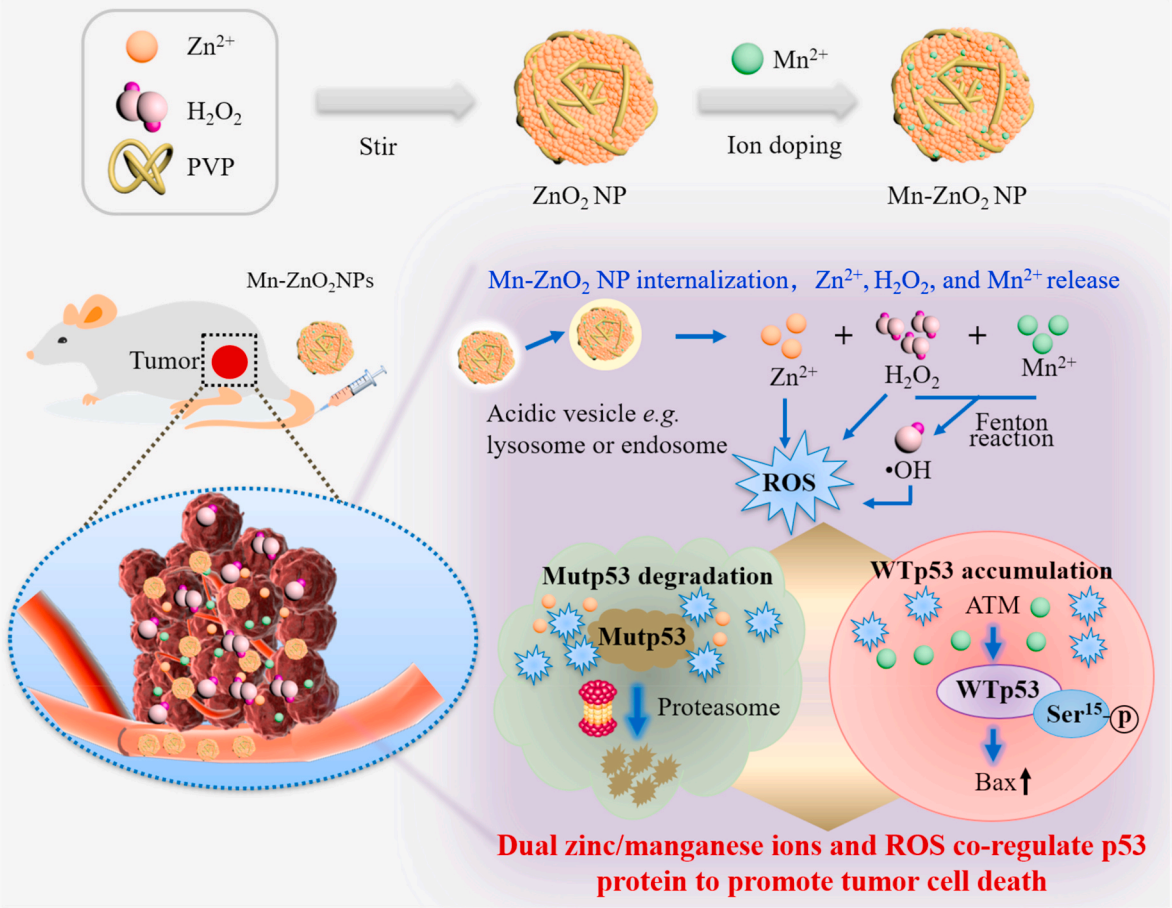

Scheme 1. Schematic illustration of the sysnthesis of carrier-free nanoprodrug for p53-mutated tumor therapy by co-delivering zinc-manganese dual ions and ROS to modulate Mutp53 degradation and WTp53 activation.

2.4. Characterization

Transmission electron microscopic (TEM) imaging was taken with a Titan Themis 200 TEM (FEI, Hillsboro, USA) at an acceleration voltage of 200 kV. UV-vis-NIR absorption spectra were obtained with a multi-detection microplate reader (BioTek Instruments, Inc., Winooski, VT). The wide-angle powder X-ray diffraction (XRD) pattern was recorded using an X-ray diffractometer (Philips X'pert XRD system) with a Cu Kα (1.5406 Å) X-ray source at 40 kV and 40 mA and a scan rate of 5° (2θ)/min (scan range: 10-90°). The size of different nanoparticles was determined by dynamic light scattering (Zetasizer 3000HS; Malvern Instruments, Worcestershire, UK). The surface area and pore size of the nanoparticles were determined by using the Brunauer-Emmett-Teller (BET), nitrogen adsorption-desorption, and Barrett-Joyner-Halenda (BJH) methods (Micromeritics, ASAP 2020), respectively. The XPS measurements were performed using a PHI-5000 CESCA system (PerkinElmer) with the radiation from an Al Kα (1486.6 eV) X-ray source. For *in vitro* MRI imaging, Mn-ZnO_2 nanoparticles with different concentrations (0, 0.1, 0.2, 0.4, and 0.8 mg/mL) were added into 200 μL tubes for MRI signal detection using an microMRI instrument (Bruker BioSpec 94/30 9.4 T MRI).

2.5. pH-responsive Mn^{2+}, Zn^{2+}, and H_2O_2 release from Mn–ZnO_2 NPs

To detect the acid-induced release of Mn^{2+} and Zn^{2+}, the Mn–ZnO_2 NPs were dialyzed against the buffer solutions at a specified pH (7.4 or 5.5). The dialysates were collected at predetermined time points and the released Mn^{2+} and Zn^{2+} were respectively detected by inductively coupled plasma mass spectrometry (ICP-MS).

The release of H_2O_2 from Mn-ZnO_2 NPs induced by acid was determined with a quantitative peroxide assay kit with a characteristic absorbance peak at 560 nm upon reaction with H_2O_2. Briefly, Mn-ZnO_2 NPs were dissolved in the buffer solutions at specified pH (7.4 or 5.5) and gently stirred for 1 h. Then, 20 μL of the above solution was mixed with the working reagent (200 μL) in the wells of 96-well plates. The UV-vis absorption spectra were measured using a multi-detection microplate reader.

2.6. •OH generation by Mn^{2+}-driven Fenton-type reaction

MB degradation-based assay was used to evaluate the •OH generation. More specifically, 5 μg/mL MB was mixed with Mn-ZnO_2 or ZnO_2 suspension (200 μg/mL) and 25 mM $NaHCO_3$ under respective pH (7.4 or 5.5) conditions. After 3 h, the UV-vis absorption in the wavelength range from 300 to 800 nm for each sample was recorded using a multi-detection microplate reader. In addition, the UV-vis absorption spectra of Mn-ZnO_2 NPs at a series of concentrations (0-200 μg/mL) dissolved in the acetate buffer (pH = 5.5) containing 5 μg/mL MB were also obtained. For the kinetic analysis, the experiments were carried out in the acetate buffer (pH = 5.5) containing MB (5 μg/mL) and Mn-ZnO_2 NPs (200 μg/mL) and the corresponding absorption spectra were recorded at the designated time points (0-180 min).

Furthermore, electron spin resonance (ESR) spectra were also obtained to detect •OH production by ZnO_2 or Mn-ZnO_2 NPs (200 μg/mL) at specified pH conditions (pH 7.4 or 5.5). The samples were pipetted into the capillary tubes. The ESR signals were recorded using a Bruker EMX ESR spectroscope with the following settings: 9.872 GHz microwave frequency, 6.375 mW microwave power, 100.00 kHz modulation

frequency, and 1.00 G modulation amplitude.

2.7. Intracellular Zn^{2+} and Mn^{2+} detection

ZnAF-2 DA as a cell-permeable fluorescent probe for Zn^{2+} was used to detect the intracellular Zn^{2+} level. After incubation with Zn^{2+} or Mn-ZnO_2 NPs for 4 h, the MDA-MB-231 cells were stained with Zn^{2+} dye (5 μM) and 4′,6-diamidino-2-phenylindole (DAPI) successively. Then, the fluorescence images were collected with the Nikon 80i epi-fluorescence microscope at Ex/Em = 488/530 nm for Zn^{2+} dye, and Ex/Em = 360/460 nm for DAPI.

To quantitatively detect the intracellular Mn^{2+} and Zn^{2+} level, MDA-MB-231 cells incubated with Mn-ZnO_2 NPs for 4 h were digested and treated with aqua regia. Quantitative analysis of Zn and Mn element was carried out by ICP-MS. The contents of Zn and Mn in the cells was calculated as nanogram per 1000 cells.

2.8. In vitro cellular ROS detection and anticancer performance

The MDA-MB-231 cells cultured in 6-well plates were incubated with Mn-ZnO_2 NPs for 4 h. Then, the cells were incubated for 20 min at 37 °C with DCFH-DA (for total ROS detection, Ex/Em = 488/530 nm) or MitoROS OH580 (for •OH detection, Ex/Em = 540/590 nm) in the Opti-MEM without FBS and antibiotics. After gentle rinsing with sterile PBS for three times, fluorescence images of the cells were obtained with the Nikon 80i epi-fluorescence microscope.

The cell-killing efficiency of Mn-ZnO_2 NPs was measured by 3-(4,5-dimethylthiazol-2-yl)-2,5-diphenyltetrazolium bromide (MTT) assay. Briefly, MDA-MB-231 cells seeded and cultured in 96-well plates for 24 h at 37 °C were respectively incubated with ZnO_2 or Mn-ZnO_2 at gradient concentrations. After incubation for 24 h, 20 μL of MTT (5 mg/mL in PBS) was added into each well. Upon removal of the media, 150 μL of DMSO was added to extract the formazan under gently shaking for 5 min, and the optical density (OD) at 590 nm was recorded with a microplate reader. Similarly, the *in vitro* anticancer activity of H_2O_2, Zn^{2+}, Mn^{2+}, Zn^{2+} plus Mn^{2+}, or Mn^{2+} plus H_2O_2 (with the same concentration) was also examined.

Live/dead staining (*i.e.*, calcein-AM/PI) was also performed to study the *in vitro* anticancer activity of Mn-ZnO_2 NPs. The MDA-MB-231 cells cultured in 6-well plates were treated with Zn^{2+} plus Mn^{2+}, ZnO_2 or Mn-ZnO_2, respectively. After incubation for 6 h, the cells were stained with calcein-AM/PI and examined under the Nikon 80i epi-fluorescence microscope.

2.9. Ubiquitination analysis of mutant p53

Following previous studies [23,34], the lysates of MDA-MB-231 cells after the treatment with Mn-ZnO_2 NPs without or with the presence of MG132 (10 μM) for 6 h were subjected to immunoprecipitation with BeaverBeads™ Protein A/G kit (BEAVER Biomedical, Suzhou, China) by using the antibody p53 (DO-1, 1 μg per sample). The pull-down complex was detected by western blotting with mutant p53 (ab32049, 1:1000 dilution), the Ubiquitin (ab134953, 1:1000 dilution) and K48-Ub (ab140601, 1:1000 dilution) antibodies.

2.10. Establishment of tumor xenograft model

Female Balb/c nude mice (6-8 weeks old, ~20 g) purchased from Huafukang Biological Technology Co. Ltd (Beijing, China) were used to generate the MDA-MB-231 xenograft tumor models. Briefly, MDA-MB-231 cells (5×10^6) suspended in 100 μL of PBS were subcutaneously injected to the back of each mouse. When the tumor volume reached ~80 mm^3, the mice were used for *in vivo* experiments. All animal experiments were carried out in accordance with the guidelines evaluated and approved by the ethics committee of Hebei University of Technology.

2.11. In vivo biodistribution and MRI imaging

The biodistribution of Mn-ZnO_2 NPs in the tumor and major organs (heart, liver, spleen, lung, and kidney) was evaluated in the tumor-bearing mice (n = 3). Mn-ZnO_2 NPs at the dose of 5 mg/kg were intravenously (*i.v.*) injected into the MDA-MB-231 tumor-bearing mice. Then, the mice were sacrificed at different time intervals (0, 4, 12, and 24 h), and the dissected tissues were weighed, homogenized, and treated with aqua regia. Quantitative analysis of Zn and Mn element was carried out with ICP-MS. The biodistribution of Zn and Mn in different tissues was calculated as the percentage of injected dose per gram of tissue (% ID/g).

For MRI imaging, MDA-MB-231 tumor-bearing mice were intravenously injected with Mn-ZnO_2 NPs at a dose of 5 mg/kg. The coronal and transverse plane MRI images at 0, 4, 12, and 24 h were obtained by a using an microMRI instrument (Bruker BioSpec 94/30 9.4 T MRI).

2.12. In vivo therapeutic effect of Mn–ZnO_2 NPs

In order to evaluate the *in vivo* therapeutic effect of Mn-ZnO_2 NPs, MDA-MB-231 tumor-bearing mice were stochastically divided into four groups (n = 5): (1) saline, (2) Zn^{2+} plus Mn^{2+} (with 1.21 mg/mL $ZnCl_2$ and 0.25 mg/mL $MnCl_2$, 100 μL), (3) ZnO_2 (1 mg/mL, 100 μL), and (4) Mn-ZnO_2 (1 mg/mL, 100 μL). During the therapeutic treatment, the mice received various treatments *via i.v.* Injection every 2 days (a total of 8 injections received for the entire treatment period). The body weight and tumor volume were also recorded every 2 days up to 16 days. The tumor volume was calculated according to the following formula: tumor volume = length × $width^2/2$. By the time of sacrificing, the tumors and all major organs were collected and processed for histological analysis upon hematoxylin & eosin (H&E) staining of their cross-sections. The ROS level in tumor tissues was assessed by staining the tissue cross-sections with dihydroethidium (DHE) (20 mM, Invitrogen) and then examining with the Nikon 80i epi-fluorescence microscope. The obtained fluorescence images of randomly selected fields (n = 5) were analyzed for fluorescence intensity using the NIH ImageJ software (1.46r).

2.13. TUNEL assay

At 48 h after the last administration, tumors with various treatments were performed for TUNEL assay (One Step TUNEL Apoptosis Assay Kit, C1088, Beyotime). Briefly, 4-μm thick paraffin sections of the resected tumors were dewaxed in xylene and rehydrated with graded ethanol solutions prior to the treatment with proteinase K for 30 min at 37 °C. Then, the sections were washed with PBS for three times and then incubated with the TUNEL reaction mixture for 60 min at 37 °C in a humidified chamber. After rinsing with PBS, the sections were stained with DAPI for nuclei, and then examined under the Nikon 80i epi-fluorescence microscope.

2.14. Western blotting

Proteins of MDA-MB 231 cells (at 12 h after treatment) or tumor tissues (at 48 h after last injection) from tumor-bearing mice were extracted and separated using 8-15% sodium dodecyl sulfate polyacrylamide gel electrophoresis (SDS-PAGE). The separated proteins were transferred to the polyvinylidene fluoride membranes and then incubated with 5% fat-free milk in PBS-Tween (0.2%) for 1 h to block the nonspecific binding. After incubation with appropriate primary antibodies, the membranes were washed three times with PBS-Tween, blotted with secondary antibodies conjugated with horseradish peroxidase for 1 h, and then imaged with the gel imaging system (Tanon-5200Multi). The primary antibodies used in this study were anti-mutant p53 (ab32049, 1:1000 dilution), anti-wildtype p53 (bs-0033R, 1:500 dilution), anti-phospho p53 (S15, ab278683, 1:10000 dilution), anti-

ATM (BA0655-2, 1:2000 dilution), anti-phospho ATM (S1981, BM4008, 1:1000 dilution), anti-Bax (ab32503, 1:1000 dilution), and anti-GADPH (ab9485, 1:2500 dilution).

2.15. Quantitative real-time PCR (qPCR)

RNA was extracted from the cells or tumor tissues and the expression of selected genes was then detected with a real-time quantitative PCR instrument (QuantStudio 1, ThermoFisher Scientific) according to the manufacturer's instructions. The gene expression level was normalized with β-actin (housekeeping gene) and presented as average ± standard deviation from duplicates or triplicates of the repeated experiments. The primers used in the qPCR analysis were listed in Table S1.

2.16. Statistical analysis

All experiments were repeated at least 3 times and presented as the mean ± SD. Significant differences among groups were determined by one-way ANOVA with Tukey multiple comparison tests. Statistical significance was set at *p < 0.05, **p < 0.01.

3. Results and discussion

3.1. Synthesis and characterization of Mn-ZnO_2 nanoprodrug

ZnO_2 NPs were synthesized from zinc acetate ($Zn(OAc)_2$) by reacting with H_2O_2 at room temperature in the presence of PVP, and a relatively good yield (12.3%) was achieved (Scheme 1). During the synthesis, the presence of PVP, which complexed with zinc ions, was able to provide the protection to ZnO_2 to form stable nanostructures, thereby affecting the growth and control the uniformity of the spherical aggregates. In the absence of PVP, however, the ZnO_2 nanocrystals tended to aggregate in a noncontrollable manner, resulting in irregular round shapes (Fig. S1a) with poor storage stability (Fig. S1b). With the aid of PVP, on the other hand, the assembly of ZnO_2 nanocrystals occurred in a controlled fashion and the formed aggregates exhibited as spherical particles with relatively uniform size and good stability. Such a distinct difference most likely resulted from PVP that could lower the surface energy of ZnO_2 nanocrystals and provide stabilization to the final nanoaggregate via its entangled polymeric chains [35]. Fourier transform infrared (FTIR) spectra revealed the presence of signature absorptions at 1670

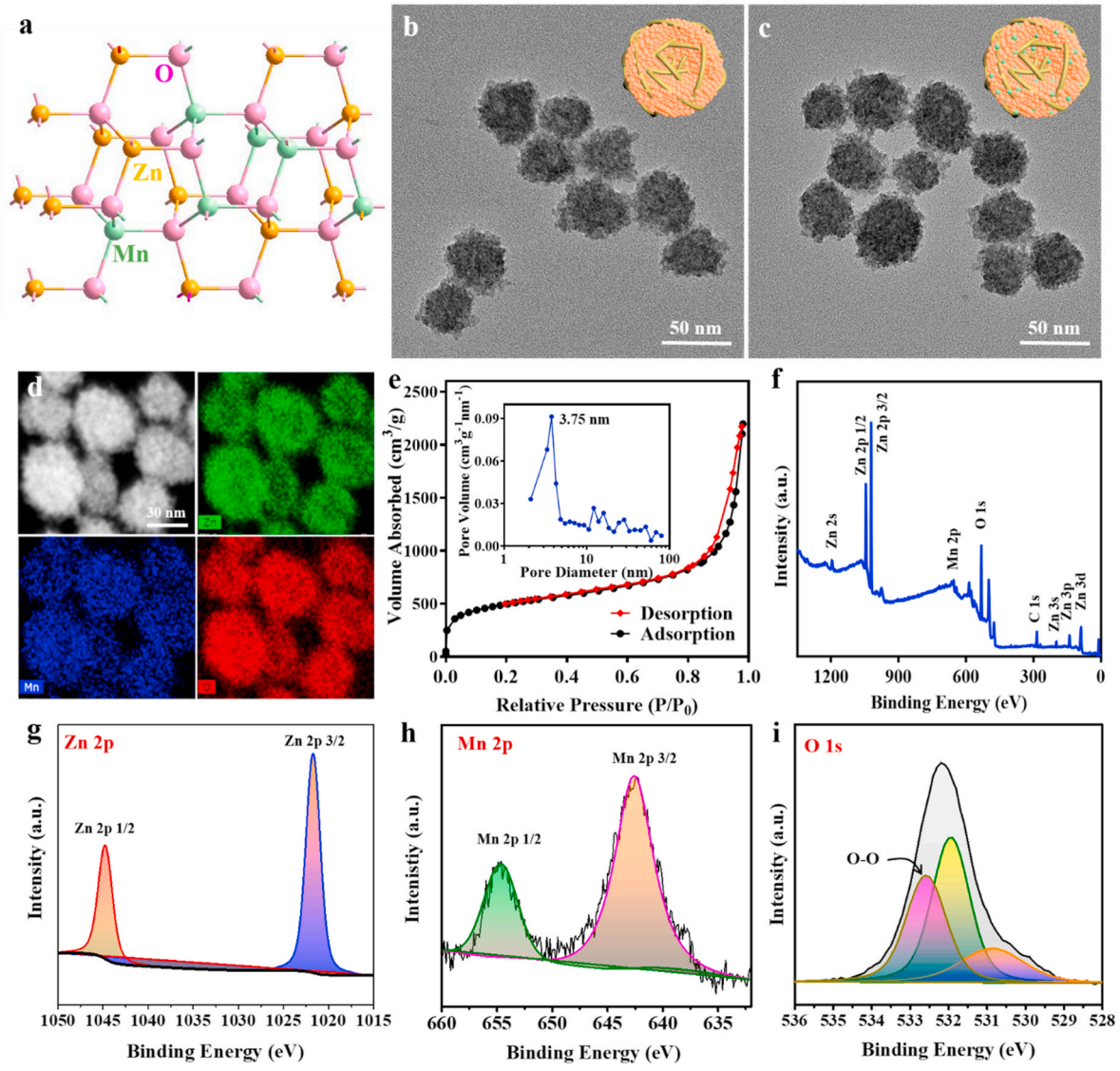

Fig. 1. Characterization of Mn-ZnO_2 NPs. (a) The crystal structure of Mn-ZnO_2 NPs. (b) Representative TEM images of ZnO_2 NPs. (c) Representative TEM images of Mn-ZnO_2 NPs. (d) STEM-HAADF image and the corresponding EDS elemental mapping of Zn, Mn, and O in Mn–ZnO_2 NPs. (e) N2 adsorption/desorption isotherm and the corresponding pore-size distribution (inset) of Mn-ZnO_2 NPs. (f–i) XPS spectra of the as-prepared Mn-ZnO_2 NPs: survey spectra (f), and high-resolution of Zn 2p (g), Mn 2p (h), and O 1s (i).

cm^{-1} (C═O stretching of PVP) and 1285 cm^{-1} (C–N stretching of PVP) [36], thereby confirming successful incorporation of PVP within the as-prepared ZnO_2 NPs (Fig. S2). To endow ZnO_2 NPs with the capability of •OH generation, WTp53 modulation, and MRI contrast, a facile cation-exchange step was therefore adopted to construct the Mn-doped ZnO_2 NPs. As a result of the similar ionic radius between Mn and Zn (0.66 Å and 0.60 Å, respectively) [33], Mn^{2+} would be readily doped into the crystal lattice of ZnO_2 *via* a gradient-driven substitution of Zn^{2+} (Fig. 1a). To determine the desirable Mn-ZnO_2 formulation for further use, ZnO_2 NPs at a constant concentration were substituted with different Mn^{2+} weight fractions. As shown in Fig. S3 and Fig. S4f, increasing Mn^{2+} in the reaction led to gradual darkening of the obtained Mn-ZnO_2 solutions, displaying the dark brownish at 80%. With the weight fraction of Mn at 50% or below, the Mn-ZnO_2 NPs retained their spherical morphology with a good uniformity (Figs. S4a–e). To correlate the Mn^{2+} weight fraction with •OH formation from H_2O_2, methylene blue (MB) was used as the indicator, which could be decomposed by •OH to lose its blue color. Interestingly, Mn-ZnO_2 NPs of 30% Mn^{2+} weight fraction exhibited the strongest •OH generation capacity (Fig. S4g). To determine the optimal Mn/Zn ratio for maximal tumor inhibitory effect, MDA-MB-231 cells were treated with Mn-ZnO_2 NPs containing different Mn^{2+} amounts and evaluated for their viability using MTT assay. To our surprise, the Mn-ZnO_2 NPs with 30% Mn^{2+} weight fraction also showed the maximal tumor cell killing efficiency (Fig. S5). Thus, Mn-ZnO_2 NPs with 30% Mn^{2+} weight fraction were particularly chosen for further experimental use.

As confirmed by transmission electron microscopy (TEM), the as-prepared ZnO_2 NPs existed as monodispersity with the spherical morphology and rather uniform size (Fig. 1b). After 30% Mn doping, the color of the obtained Mn-ZnO_2 NPs solution changed from milk white (ZnO_2 NPs suspension) into yellow-brownish (Fig. S6 inset) and the absorbance at 350 nm was also significantly increased (Fig. S6). The microstructure of obtained Mn-ZnO_2 NPs was further characterized by TEM and they remained the uniform spherical shape (Fig. 1c). As measured, the mean diameter of Mn-ZnO_2 NPs was 42.1 ± 2.5 nm, which was very comparable if not identical to that of the ZnO_2 NPs (44.2 ± 3.8 nm) (Fig. S7), and such sizes allow for prolonged circulation in the blood for enhanced extravasation into tumors [37]. Energy-dispersive X-ray spectroscopy (EDS) elemental mapping of the prepared Mn-ZnO_2 NPs confirmed the presence of Zn, Mn, and O (Fig. 1d and Fig. S8). X-ray diffraction (XRD) characterization further validated the remaining crystal structure of ZnO_2 in the Mn-ZnO_2 NPs (Fig. S9) with completely matched diffraction peaks to the typical cubic structure of nano ZnO_2 as described in the literature [38,39]. To further verify the composition of Mn-ZnO_2 NPs especially the valence state of elements, X-ray photoelectron spectroscopy (XPS) analysis was performed. The total spectrum (Fig. 1f) confirmed the presence of Zn, Mn, O elements and the bonding energy of Zn 2p, Zn 3s, Zn 3p, Mn 2p and O 1s. As shown in Fig. 1g, the two splitting peaks at 1044.8 and 1021.7 eV corresponded to the Zn 2p1/2 and Zn 2p3/2 orbits of Zn^{2+}, respectively. And the two peaks at 655.3 and 640.3 eV with a peak spacing of 15 eV in Fig. 1h were in a good agreement with Mn 2p1/2 and Mn 2p3/2 peaks of Mn^{2+}. The O 1s peak at 532.6 eV was assigned to O–O, suggesting the existence of peroxide groups (Fig. 1i). Once again, XPS results confirmed the sole presence of Zn^{2+} and Mn^{2+} in Mn-ZnO_2 NPs as the peroxide compound.

Interestingly, mesopores were identified in the as-prepared Mn-ZnO_2 NPs and the specific surface area determined from the nitrogen adsorption isotherms (Fig. 1e) was as high as 1746.4 m^2/g, clearly offering more active sites for decomposition reactions. Mapping the pore-size distribution (inset of Fig. 1e) revealed the peak pore diameter at 3.75 nm, large enough for free transport of the released ions and H_2O_2 in and out. To assure the stability of Mn-ZnO_2 NPs for future *in vitro* and *in vivo* use, additional tests were performed by extending the storage period up to 30 days. As summarized in Table S2, even incubation in the media containing 10% FBS (close to physiological conditions) for 30 days, the Mn-ZnO_2 NPs remained well dispersed without noticeable aggregation/precipitation and the size also kept similar despite a slight increase over the time (Table S2). Apparently, the demonstrated stability of Mn-ZnO_2 NPs mainly results from the presence of PVP in the nanostructures [40].

3.2. Acid-induced dual Zn-Mn ions/H_2O_2 release and •OH generation from Mn-ZnO_2 NPs

As the carrier-free nanoprodrug, we expect these Mn-ZnO_2 NPs would decompose and release the dual ions (Mn^{2+} and Zn^{2+}) and ROS in an acidic tumor microenvironment while being stable under the physiological pH of other tissues (Fig. 2a). To demonstrate such a pH sensitivity of Mn-ZnO_2 NPs, we accordingly measured the release of H_2O_2, Zn^{2+}, and Mn^{2+} from Mn-ZnO_2 NPs under the neutral (pH 7.4, physiological) or acidic (pH 5.5, tumoral) conditions. We analyzed the release of H_2O_2 from Mn-ZnO_2 NPs by using a ferrous (Fe) ion oxidation xylenol orange (XO)-based assay with the Pierce™ Quantitative Peroxide (PQP) Assay Kit [41,42]. In this assay, the peroxide, *i.e.*, released H_2O_2, can directly convert the Fe^{2+} to Fe^{3+}, which react with the XO dye to yield a purple product with a maximum absorbance at 560 nm. As shown in Fig. 2b, a significant absorption peak appeared at 560 nm upon the incubation of PQP solution with Mn-ZnO_2 NPs at pH 5.5, while only a marginal absorbance at 560 nm was seen at pH 7.4, confirming a mild acidic environment would effectively cause the generation of H_2O_2. Time-dependent release of Zn^{2+} and Mn^{2+} from Mn-ZnO_2 NPs under different pH conditions (*i.e.*, 7.4 versus 5.5) was measured by inductively coupled plasma mass spectrometry (ICP-MS), showing a rapid release of Zn^{2+} and Mn^{2+} from the Mn-ZnO_2 NPs at pH 5.5 and reaching their releasing plateau around 6 h (Fig. 2c and d). In contrast, the release of Zn^{2+} and Mn^{2+} in pH 7.4 buffer solution was rather slow with very low release rates. Interestingly, upon switching the pH from 7.4 to 5.5, the color of Mn-ZnO_2 solution (yellow-brownish) turned to colorless rapidly and the strong UV absorbance also disappeared immediately (Fig. S10a). TEM examination of the Mn-ZnO_2 NPs incubated in different pH buffers for 1 h showed that Mn–ZnO_2 NPs remained unchanged at pH 7.4 while almost completely dissociated and decomposed at pH 5.5 (Figs. S10b and c). The accelerated release of Zn^{2+} and Mn^{2+} in a mild acidic environment is most likely due to the facilitated decomposition of Mn-ZnO_2 NPs. Apparently, such a pH-sensitive decomposition of Mn-ZnO_2 NPs displays noticeable advantages for *in vivo* tumor treatment especially considering that the acidic endo/lysosomes (pH 5.0-6.0) of cancer cells [43] would similarly trigger the release of H_2O_2 and ions in an on-demand manner.

Given the paramagnetic property of Mn^{2+} [44] and the pH-dependent release of Mn^{2+}, we also compared the MR imaging signal and longitudinal (T_1) relaxivity of Mn-ZnO_2 NPs solutions with different concentrations at pH 7.4 or 5.5. As shown in the T_1-weighted MR imaging (Fig. 2e), the signal intensity detected from the Mn-ZnO_2 solutions was proportional to their concentration in a linear function at pH 5.5, while the signal intensity at pH 7.4 remained hypointense up to 0.8 mM. Additionally, the T_1 relaxation rate (γ_1) also increased drastically from 0.81 (pH 7.4) to 5.53 $mM^{-1}s^{-1}$ (pH 5.5) (Fig. 2e), revealing the unique pH-activatable MRI contrast of Mn-ZnO_2 NPs, mainly due to enhanced chemical exchange between protons and Mn^{2+} released from Mn-ZnO_2 NPs at pH 5.5. The off-to-on high MR contrast enabled by Mn-ZnO_2 NPs in response to the mild acidic conditions delivers a promising MRI modality to selectively visualize the targeted tumor with a minimum interference from surrounding healthy tissues.

Theoretically, the concurrently released Mn^{2+} and H_2O_2 from Mn-ZnO_2 NPs in an acidic environment would lead to the generation of cytotoxic •OH *via* the Fenton catalytic reaction [45–48]. To demonstrate this, electron spin resonance (ESR) spectrometry was used to detect •OH formation through the Mn-based Fenton-like reaction upon incubation of Mn-ZnO_2 NPs in the simulated acidic tumor environment. In contrast to the extremely weak ESR signals of •OH at pH 7.4, incubation of

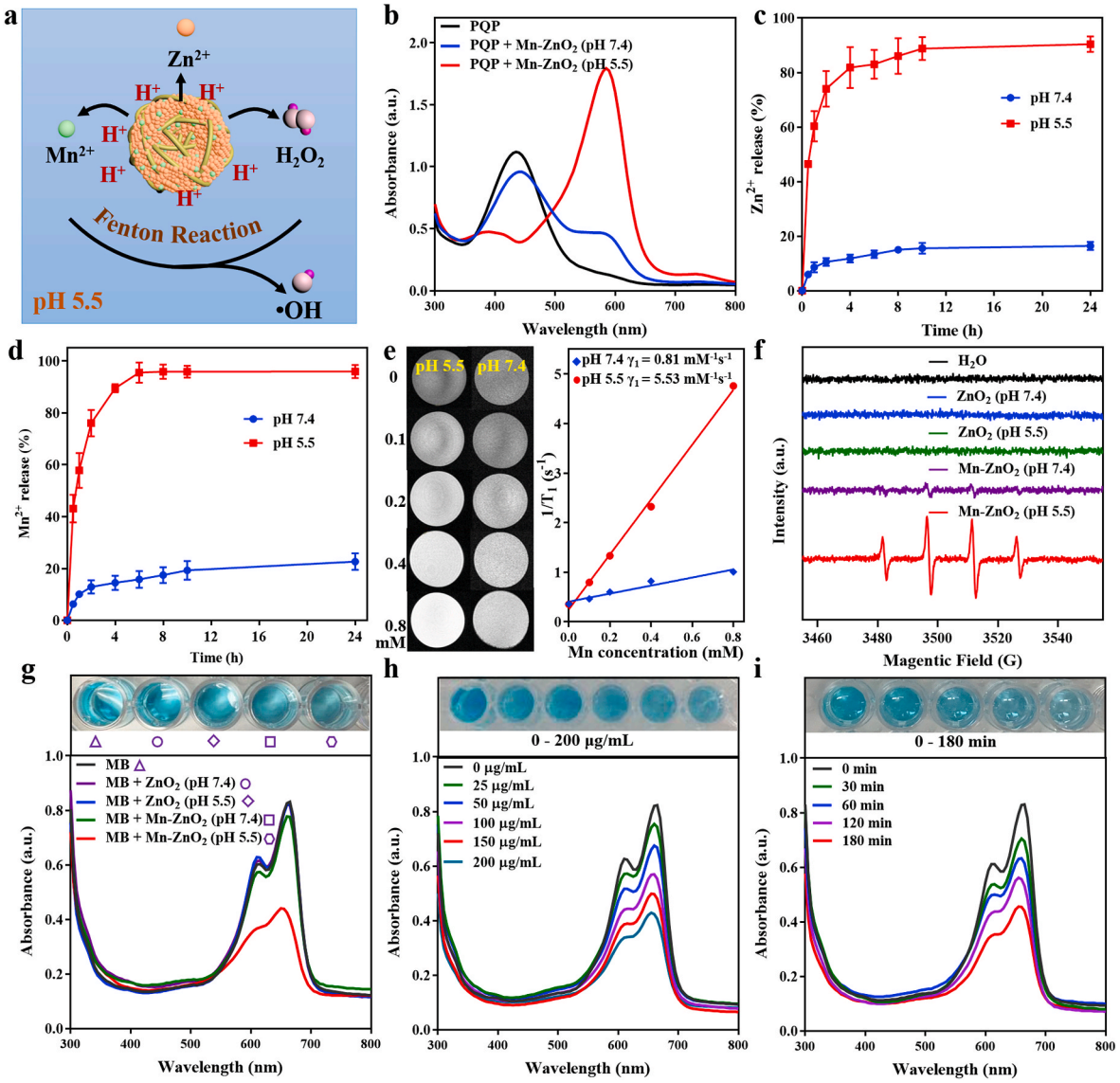

Fig. 2. The pH-responsive performances and •OH generation of Mn-ZnO_2 NPs. (a) Schematic illustration of the release of dual Zn-Mn ions and H_2O_2 and subsequent •OH generation from Mn-ZnO_2 NPs. (b) UV–vis spectra of the Pierce™ Quantitative Peroxide (PQP) solution incubated with Mn–ZnO_2 NPs at neutral (pH 7.4) or acidic (pH 5.5) conditions. Release profiles of (c) Zn^{2+} and (d) Mn^{2+} from Mn-ZnO_2 NPs at different pH conditions. (e) The MRI images (left) and γ_1 values (right) of Mn–ZnO_2 NPs under different pH conditions. (f) ESR signals detected under different conditions (H_2O, ZnO_2 NPs at pH 7.4 or 5.5, Mn-ZnO_2 NPs at pH 7.4 or 5.5). (g) The UV-vis-NIR absorption spectra of different solutions (MB, MB plus ZnO_2 NPs at pH 7.4 or 5.5, MB plus Mn-ZnO_2 NPs at pH 7.4 or 5.5). (h) The UV-vis-NIR absorption spectra of $NaHCO_3$ (25 mM)/MB (5 μg/mL) mixed solutions at pH 5.5 with the presence of Mn-ZnO_2 NPs at different concentrations. (i) The time-dependent UV-vi-NIR absorption spectra of MB reacted with 200 μg/mL Mn-ZnO_2 NPs and 25 mM $NaHCO_3$ at pH 5.5.

Mn-ZnO_2 NPs within the pH 5.5 buffer solution did cause a much stronger signal (Fig. 2f), confirming the capability of Mn-ZnO_2 NPs in efficiently generating •OH under an acidic condition. On the other hand, no detectable ESR signals were seen with ZnO_2 NPs solutions either at pH 7.4 or pH 5.5, further illustrating the importance of Mn^{2+} for •OH formation. In addition, methylene blue (MB), a dye probe that is specifically decomposed by •OH, was used to further quantify •OH formation. Consistent with ESR measurements, Mn-ZnO_2 NPs (pH 5.5) yielded the most decomposition of MB while only a marginal decomposition with Mn-ZnO_2 NPs (pH 7.4) or no change with other circumstances (Fig. 2g). Furthermore, decomposition of MB by acidified Mn-ZnO_2 NPs was both concentration- (Fig. 2h) and time-dependent (Fig. 2i). All these results affirmed the capacity and efficiency of self-generating •OH by Mn-ZnO_2 NPs under an acidic tumor-like environment.

3.3. Intracellular Zn^{2+}, Mn^{2+}, and ROS elevation by Mn-ZnO_2 NPs

As a result of the acidic (pH 5.0-6.0) endo/lysosomal environment of cancer cells, pH-sensitive Mn-ZnO_2 NPs after endocytosis should be decomposed into Zn^{2+}, Mn^{2+}, and H_2O_2 and then followed with intracellular •OH production *via* the Fenton-like reaction between Mn^{2+} and H_2O_2 (Fig. 3a). To verify the onset of such expected events, breast cancer cells (MDA-MB-231) exhibiting high p53 mutation [49] was particularly selected for the *in vitro* cellular study. To visualize the elevated intracellular Zn^{2+} level, a Zn^{2+} specific fluorescent indicator (ZnAF-2 DA) was used to stain the cells upon incubation with Mn-ZnO_2 NPs. As shown in Fig. 3b and Fig. S11, significantly higher green fluorescence was seen with the cells incubated with Mn–ZnO_2 NPs than those untreated control or treated with $ZnCl_2$. To better quantify the increases of intracellular Mn^{2+} and Zn^{2+} by Mn-ZnO_2 NPs, ICP-MS measurement was performed. Clearly, the Mn-ZnO_2 NP treatment elevated both Mn^{2+} and Zn^{2+} levels

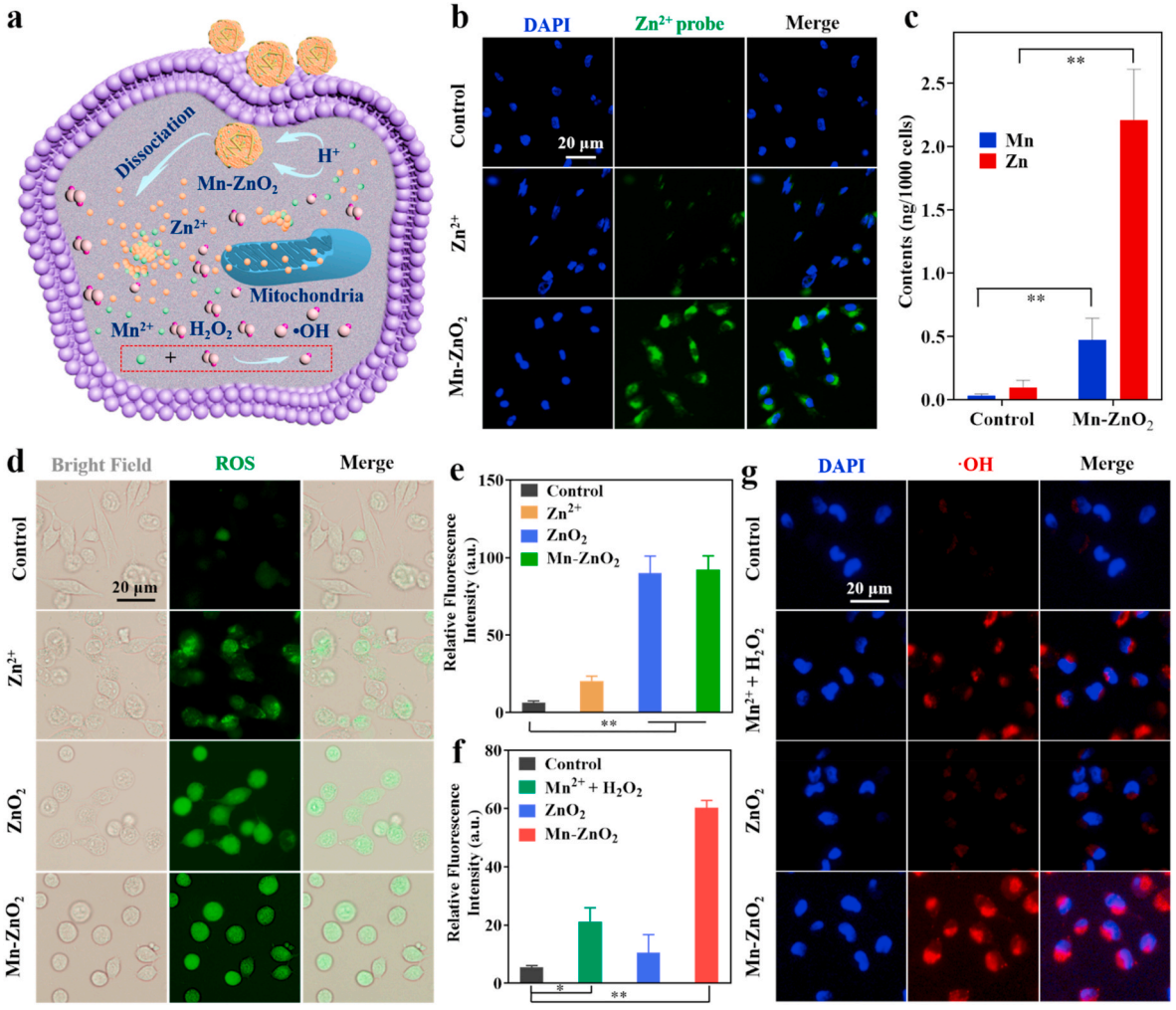

Fig. 3. Intracellular elevation of dual Zn-Mn ions and ROS by Mn-ZnO_2 NPs. (a) Schematic illustration of intracellular release of dual Zn-Mn ions and H_2O_2 and subsequent •OH generation from Mn-ZnO_2 NPs. (b) Fluorescence images of MDA-MB-231 cells stained with Zn^{2+} dye (green) after incubation with $ZnCl_2$ or Mn-ZnO_2 NPs for 4 h. (c) Quantification of intracellular Zn^{2+} and Mn^{2+} elevated by Mn-ZnO_2 NPs using ICP-MS analysis. $^{**}p < 0.01$. (d) Fluorescence images of ROS production (green) in MDA-MB-231 cells after various treatments (non-treated control, $ZnCl_2$, ZnO_2 NPs, or Mn-ZnO_2 NPs). (e) Semi-quantification of the DCF fluorescence intensity in MDA-MB-231 cells after various treatments. $^{**}p < 0.01$. (f) Semi-quantification of the fluorescence intensity of •OH probe in MDA-MB-231 cells after various treatments. $^{*}p < 0.05$ and $^{**}p < 0.01$. (g) Fluorescence images of •OH generation in MDA-MB-231 cells after various treatments (non-treated control, $MnCl_2$ + H_2O_2, ZnO_2, or Mn-ZnO_2 NPs).

dramatically, about 189.7 and 690.5 times of the nontreated controls, respectively (Fig. 3c), implying the efficiency in releasing ions from Mn-ZnO_2 NPs within a tumor cell environment.

Next, the boosted level of intracellular ROS caused by released H_2O_2 was detected using 2′,7′-dichlorofluorescin diacetate (DCFH-DA) as the indicator. Upon cellular uptake, DCFH-DA undergoes deacetylation by intracellular esterase to yield nonfluorescent DCFH, which can be oxidized by ROS to emit green fluorescence [50–52]. As demonstrated in Fig. 3d, MDA-MB-231 cells incubated with $ZnCl_2$ displayed relatively stronger green fluorescence compared to those nontreated cells. The enhanced intracellular ROS upon Zn^{2+} exposure might be mainly attributed to Zn^{2+}-induced mitochondrial ROS production [53–56]. As expected, the cells incubated with either ZnO_2 NPs or Mn-ZnO_2 NPs yielded comparable green fluorescence but much higher intensity than that of nontreated controls and even Zn^{2+}-challenged ones. Such results suggest intracellular ROS elevation is the combined effect of H_2O_2 and Zn^{2+}. Semi-quantification of the fluorescence intensity using ImageJ revealed that Mn-ZnO_2 group was approximately 14.4 times of the control group. Above results confirmed the ROS generation capability of Mn-ZnO_2 NPs in cancer cells *via* both endogenous (by Zn^{2+}) and exogenous (by H_2O_2) avenues. Considering that DCFH-DA reacts with all ROS including H_2O_2 and •OH [57], a novel live-cell permeant hydroxyl radical probe (MitoROS™ OH580) with a good selectivity toward •OH was used to evaluate the intracellular •OH level, which reacts with MitoROS™ OH580 to rapidly generate the red fluorescence [58]. Compared to negligible fluorescence in other groups (no treatment or ZnO_2 NPs), cells treated with $MnCl_2$ and H_2O_2 did show red fluorescence, but still relatively weak (Fig. 3g). In contrast, the cells with Mn-ZnO_2 NPs had much stronger red fluorescence, about 10.9 times of the nontreated controls (Fig. 3f), suggesting effective generation of •OH within the tumor cells through the Fenton-like reaction from the released Mn^{2+} and H_2O_2. The noted difference in •OH generation between $MnCl_2$/H_2O_2 and Mn-ZnO_2 NPs might mainly come from the limited and varying transport efficiency of Mn^{2+} and H_2O_2 from exogenous $MnCl_2$/H_2O_2 through the cell membrane, and on the other hand also highlighted the advantages of Mn-ZnO_2 NPs in terms of effective intracellular delivery and on-demand release of Mn^{2+}/Zn^{2+} and H_2O_2 for desired biological functions while minimizing the unwanted side effects.

3.4. In vitro antitumor effect of Mn-ZnO_2 NPs via modulation of p53 protein and enhancement of •OH formation

Encouraged by the above results, we further hypothesized that the released Zn^{2+}, Mn^{2+}, and ROS might be able to elicit Mutp53 degradation and activate the ATM-WTp53-Bax signal pathway, synergistically inducing the death of p53 mutant tumor cells (Fig. 4a). To verify this, we firstly investigated whether Mn-ZnO_2 NPs could cause Mutp53 degradation in the highly p53 mutant MDA-MB-231 cells. In comparison to negligible Mutp53-degrading capacity in other groups (no treatment or Mn^{2+}), both ZnO_2 and Mn-ZnO_2 NPs markedly decreased the level of Mutp53 (Fig. 4b and c). However, $ZnCl_2$ at an equivalent zinc-concentration was much less effective in causing Mutp53 degradation, most likely due to its poor ability to diffuse through the cell membrane via ion channels [29]. Meanwhile, H_2O_2 alone was also able to reduce the Mutp53 level to some extent. These results confirmed the dependence of Mutp53 degradation on Zn^{2+} and H_2O_2 released from Mn-ZnO_2 NPs but independent of Mn^{2+}. To better interrogate the underlying mechanism, especially the involvement of intracellular oxidative level, we examined the Mutp53 protein level in MDA-MB-231 cells treated with Mn-ZnO_2 NPs with or without the presence of a global antioxidant N-acetyl cysteine (NAC), which was expected to abolish the ROS

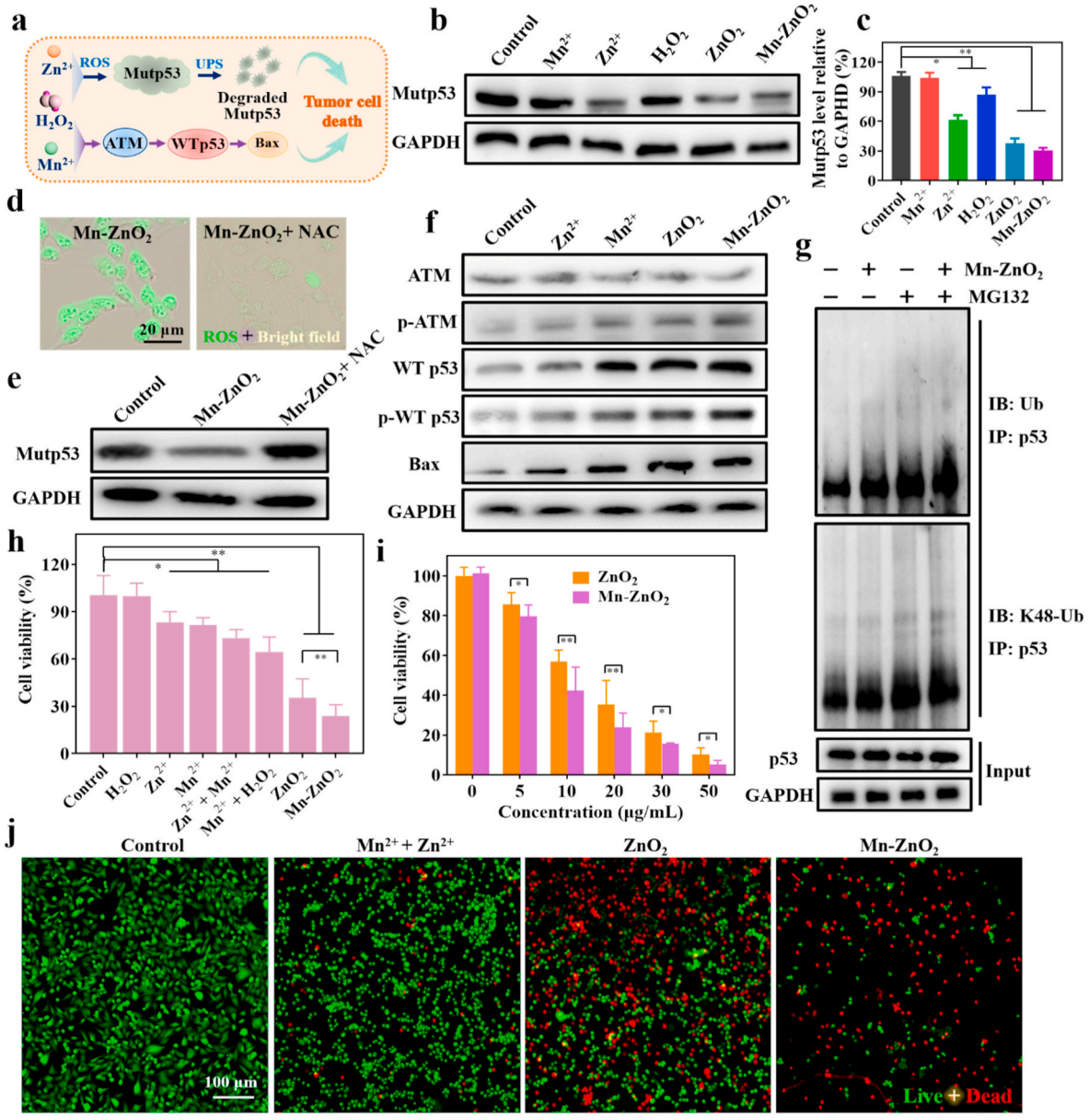

Fig. 4. Mn-ZnO_2 NP-mediated modulation of p53 proteins and cell-based killing efficiency. (a) The proposed mechanism on tumor cell death induced by Mn-ZnO_2 NPs via the regulation of p53 proteins. (b) Western blotting of Mutp53 in MDA-MB-231 cells after various treatments (non-treated control, $MnCl_2$, $ZnCl_2$, H_2O_2, ZnO_2 NPs, or Mn-ZnO_2 NPs). (c) Semi-quantification of the Mutp53 level shown in b. $^*p < 0.05$, $^{**}p < 0.01$. (d) Fluorescence images of ROS production in MDA-MB-231 cells after treated with Mn-ZnO_2 NPs or Mn-ZnO_2 NPs + NAC. (e) Western blotting of Mutp53 in MDA-MB-231 cells after the Mn-ZnO_2 NPs treatment without or with NAC. (f) Western blotting of ATM, WTp53, and Bax in MDA-MB-231 cells after various treatments (non-treated control, $ZnCl_2$, $MnCl_2$, ZnO_2 NPs, or Mn-ZnO_2 NPs). (g) Western blotting (WB) of total ubiquitination (Ub) and K48-polyubiquitination (K48-Ub) of the immunoprecipitated (IP) p53 in MDA-MB-231 cells after the Mn-ZnO_2 NPs treatment without or with MG132. (h) Viability of MDA-MB-231 cells after various treatments. Data are expressed as mean ± SD (n = 6). $^*p < 0.05$, $^{**}p < 0.01$. (i) Viability of MDA-MB-231 cells treated with ZnO_2 NPs or Mn–ZnO_2 NPs, respectively. Data are expressed as mean ± SD (n = 6). $^*p < 0.05$, $^{**}p < 0.01$. (j) Fluorescence images of MDA-MB-231 cells after different treatments (non-treated control, Zn^{2+} + Mn^{2+}, ZnO_2 NPs, or Mn-ZnO_2 NPs). Cells were stained live (green) with calcein-AM and dead (red) with PI.

elevated by Mn-ZnO_2 NPs. Notably, the ROS level was indeed dramatically reduced by NAC (Fig. 4d). As such, the degradation of Mutp53 by Mn-ZnO_2 NPs was fully rescued (Fig. 4e and Fig. S12). Thus, intracellular ROS elevation is crucial toward Mutp53 proteasomal degradation induced by Mn-ZnO_2 NPs. To further determine whether such a the decreased Mutp53 level was from a reduced transcription, we conducted qPCR analysis to the cells with different treatments. Interestingly, no difference in Mutp53 mRNA expression was seen with ZnO_2 or Mn-ZnO_2 NPs from that of non-treated controls (Fig. S13), indicating that neither Zn^{2+} nor ROS released from Mn-ZnO_2 NPs altered the transcription of Mutp53 and the corresponding Mutp53 reduction most likely occurred through the post-translational degradation. Thus, the involvement of ubiquitination-mediated proteasome-degradation of Mutp53 [34] was verified using the MG132, a potent and cell-permeable proteasome inhibitor [59]. As shown in Fig. S14, MG132 could completely abolish the ability of Mn-ZnO_2 to degrade mutp53. As confirmed, Mn-ZnO_2 NPs enhanced ubiquitination and K48 polyubiquitination of total cellular proteins (Fig. S15) and of Mutp53 (Fig. 4g) in MDA-MB-231 cells. MG132 treatment further increased the level of Mutp53 ubiquitination and particularly K48 polyubiquitination associated with proteasomal degradation [60]. Above results proved that Mn-ZnO_2 NPs degraded Mutp53 protein through the post-translational degradation *via* the ubiquitination-dependent proteasomal pathway.

The possible activation of ATM-WTp53-Bax pathway in MDA-MB-231 cells by Mn-ZnO_2 NPs was also investigated by examining the essential protein levels. In comparison to the low improvement of WTp53 accumulation by Zn^{2+} stimulation alone, noted accumulation of WTp53 was observed with Mn^{2+}, ZnO_2 NPs, and Mn-ZnO_2 NPs treatment, particularly Mn-ZnO_2 NPs, which showed about 4-fold increase (Fig. 4f and Fig. S16). Meanwhile, Mn-ZnO_2 NPs also led to marked activation of the ATM-WTp53-Bax pathway by elevating the marker proteins of phosphorylated ATM (Ser1981, p-ATM), total WT p53, phosphorylated WTp53 (Ser15, p-WTp53), and Bax (Fig. 4f and Fig. S16). To our surprise, p-ATM, total WTp53, p-WTp53, and Bax were also augmented in the ZnO_2 NPs-treated group while the total ATM levels remained unaltered, which might be attributed to the activation of ATM autophosphorylation by intracellular ROS [61]. More importantly, the highest WTp53 accumulation detected in MDA-MB-231 cells with Mn-ZnO_2 NPs implied the potential for enhanced cellular apoptosis. Analyses of several key mRNAs by qPCR (Fig. S13) revealed that the ATM mRNA expression level was not affected by Mn-ZnO_2 NPs, consistent with previous report on the involvement of ATM kinase in p53 phosphorylation through a post-translational modification [62,63]. Whereas the increase of WTp53 and Bax mRNA level may come from the ROS-mediated p53 gene upregulation and the subsequent transcriptional regulation of Bax expression [64]. The obtained data affirmed that the release of Mn^{2+} and ROS from Mn-ZnO_2 NPs within tumor cells was able to activate the ATM-WTp53-Bax pathway by triggering the ATM phosphorylation, following with stabilization and accumulation of WTp53, and eventually inducing the Bax anticancer effect.

Increasing evidence has shown that the highly stabilized Mutp53 favors the growth and survival of cancer cells, whereas WTp53 exhibits the opposite effect [3]. To this end, the Mn-ZnO_2 NP-induced dual events, *i.e.*, degrading Mutp53 and activating WTp53, were expected to cause more destruction of p53 mutant cancer cells. (*i.e.*, low cell viability). To validate this assumption, several selected cell lines with Mutp53, WTp53 or p53 absence were respectively treated with Mn-ZnO_2 NPs. As shown in Fig. S17, Mn-ZnO_2 NPs caused a significant reduction of cell viability to all three p53 mutant cell lines (MDA-MB-231, ES-2, and MIA PaCa-2) (over 70% cell killing efficiency) in comparison to two p53 wild-type cell lines (A549 and Hela) and one p53 absent cell line (4T1) (only 30-40% cell killing). Next, the killing efficacy of MDA-MB-231 cells by Mn-ZnO_2 NPs *via* p53 protein regulation and •OH generation was further evaluated. As shown in Fig. 4h, H_2O_2, Zn^{2+}, or Mn^{2+} alone yielded relatively low cell killing efficacy (11.6%, 16.9%, or 18.5%, respectively), lower than the synergistic combination treatments such as Zn^{2+} plus Mn^{2+} (26.7%) or Mn^{2+} plus H_2O_2 (35.4%). The highest cell killing efficacy was achieved with either ZnO_2 or Mn-ZnO_2 NPs (64.7% and 76.1%, respectively). Such a high killing efficacy most likely comes from the ready uptake of stable nanoparticles (ZnO_2 or Mn-ZnO_2 NPs) by MDA-MB-231 cells and then intracellular rapid release of ions and ROS upon decomposition. The noted further enhancement of cell killing by Mn-ZnO_2 NPs was a combinatory anticancer effect from p53 protein and •OH, which were regulated by the pH-responsive release of H_2O_2 and Zn-Mn dual ions in the acidic endo/lysosomes [43]. Next, the concentration-dependent anticancer effect of ZnO_2 or Mn-ZnO_2 NPs was also evaluated. Apparently, the cell killing capacity closely correlated with the concentration of ZnO_2 or Mn-ZnO_2 NPs and reached as high as 94% cell killing with 50 μg/mL Mn-ZnO_2 NPs (Fig. 4i). To further confirm the anticancer effect of Mn–ZnO_2 NPs *via* causation of cell death, the cells were fluorescently stained with calcein-AM (live, green) and PI (dead, red). Mn–ZnO_2 NPs did lead to significant cell death compared to either Zn^{2+} plus Mn^{2+} or ZnO_2 NPs (Fig. 4j). In addition, Mn-ZnO_2 NP-induced degradation of mutp53 and wild-type p53 accumulation in MDA-MB-231 cells also caused the cell cycle arrest at the G2M phase (Fig. S18), consistent with previous evidence [23]. Taken together, the obtained results demonstrated that Mn-ZnO_2 NPs could induce Mutp53 degradation via the released Zn^{2+} and ROS, activate WTp53 mainly *via* the released Mn^{2+}, and promote cytotoxic •OH generation *via* the Fenton reaction, which synergistically eradicated the p53-mutated tumor cells.

3.5. *In vivo* therapeutic effect of Mn-ZnO_2 NPs in p53-mutated tumor

In view of the anticancer effects of Mn-ZnO_2 NPs with cell culture, efforts were made to further understand their efficacy in *in vivo* therapy of p53-mutated cancer on MDA-MB-231-tumor-bearing mice. Following the cellular study results (Fig. 3), it is reasonable to anticipate that Mn-ZnO_2 NPs could accumulate in the tumors *via* the enhanced permeability and retention (EPR) effect [65]. Thus, tumor-specific accumulation and biodistribution of Zn and Mn were first analyzed to the organs/tissues (heart, liver, spleen, lung, kidney, and tumor) harvested from the MDA-MB-231-tumor-bearing mice upon *i.v.* Injection of Mn-ZnO_2 NPs *via* ICP-MS. As shown in Fig. 5a and b, Mn-ZnO_2 NPs could efficiently accumulate in the tumors and release dual Zn^{2+} and Mn^{2+} ions with the respective enrichment rate of 32.1%, 47.1%, and 40.6% for Zn and 10.7%, 42.5%, and 25.3% for Mn at 4, 12, and 24 h after *i.v.* Injection. At 12 h post-injection, both Zn^{2+} and Mn^{2+} in the tumors reached their maximum levels, demonstrating the good stealthy capability of Mn-ZnO_2 NPs in circulation for better tumor accumulation. Thanks to the paramagnetic Mn^{2+} and its concentration-resolved enhancement of MR signal (Fig. 2e), *in vivo* MR imaging was also performed to verify the high tumor accumulation of Mn-ZnO_2 NPs (Fig. 5c). Compared to negligible MRI signal (*i.e.*, baseline) prior to *i.v.* Injection of Mn-ZnO_2 NPs, intense MRI signal in the tumor region was seen 12 h post-injection of Mn-ZnO_2 NPs, *i.e.*, approximately 1.6 times of the baseline (Fig. 5d). Both biodistribution and MR imaging results confirmed the high accumulation of Mn-ZnO_2 NPs in the tumor site.

With the demonstrated advantages of Mn-ZnO_2 NPs, *i.e.*, high tumorous accumulation, on-demand (low pH triggered) release of dual ions (Mn^{2+}, Zn^{2+}) and ROS, effective modulation of p53 protein, efficient generation of highly toxic •OH, as well as pH-activated MR imaging modality, the therapeutic effect on p53-mutated MDA-MB-231 tumors was accordingly performed (Fig. 5e). Tumor bearing mice were randomly divided into four groups (n = 5) and respectively treated with: 1) saline, 2) Zn^{2+} + Mn^{2+}, 3) ZnO_2 NPs, and 4) Mn-ZnO_2 NPs. Time-resolved tumor progression was monitored by recording the tumor images (Fig. 5f) and measuring the tumor volume. As shown in Fig. 5g, Zn^{2+} plus Mn^{2+} exhibited negligible therapeutic effect on tumor inhibition with no statistical difference from controls (saline only). In contrast to a partial tumor suppression by ZnO_2 NPs, significantly reduced tumor growth was observed with the Mn-ZnO_2 NPs treatment,

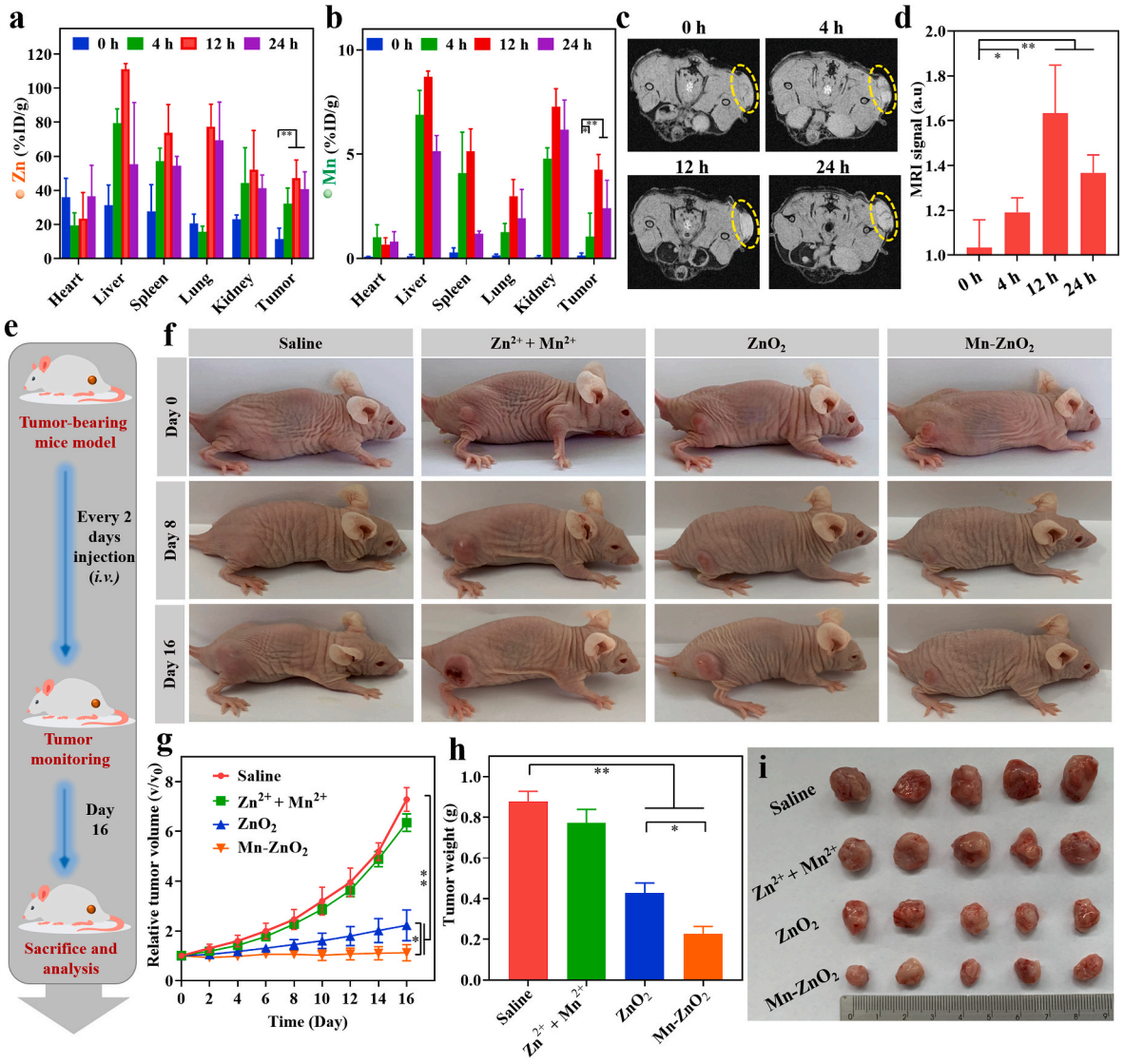

Fig. 5. Biodistribution and therapy effect of Mn-ZnO_2 NPs on p53-mutant tumor. Biodistribution of (a) Zn and (b) Mn (% ID of Zn or Mn per gram of tissues) in major organs and tumor after intravenous administration of Mn-ZnO_2 NPs for different time intervals (0, 4, 12, and 24 h) (n = 3). *$p < 0.05$, **$p < 0.01$. (c) *In vivo* T_1-weighted MRI images of MDA-MB-231 tumor-bearing mice after intravenous injection of Mn-ZnO_2 NPs for different time intervals (0, 4, 12, and 24 h). Yellow circle indicated the tumor region. (d) Average intensity of MRI signals at the tumor site. *$p < 0.05$, **$p < 0.01$. (e) Schematic illustration of the experimental setup for *in vivo* p53-mutated tumor therapy using Mn-ZnO_2 NPs. (f) Photos of the tumorous region in the mice with different treatments (saline, Zn^{2+} + Mn^{2+}, ZnO_2 NPs, or Mn-ZnO_2 NPs). (g) Time-dependent tumor progression (volume-based) in mice with different treatments. (h) Terminal weights of tumors resected from mice with different treatments. *$p < 0.05$, **$p < 0.01$. (i) Photos of the terminal tumors harvested from mice with different treatments (day 16).

showing no change of tumor volume throughout the experimental period. The terminal weight of excised tumors agreed well with the tumor volume measurements (Fig. 5h and i), and again Mn-ZnO_2 NPs yielded the highest antitumor capacity.

To evaluate the cell phenotype within Mn-ZnO_2 NP-treated tumors, the cross-sections of tumors were stained with hematoxylin and eosin (H&E) and terminal deoxynucleotidyl transferase-mediated nick end labeling assay (TUNEL). H&E staining revealed that Mn-ZnO_2 NP-treatment led to significant necrosis and anucleate of cells within the treated tumors (Fig. 6a and inset). Similarly, the TUNEL assay also showed the highest cell apoptosis (82.1%) occurred to the Mn-ZnO_2 NP-treated tumors (Fig. 6b and c). To determine whether Mn-ZnO_2 NPs could elevate the tumoral ROS level, cryosections of tumors were stained with dihydroethidium (DHE) probe, which can be oxidized into ethidium by intracellular ROS and then intercalated into DNA to produce red fluorescence [66]. As shown in Fig. 6e, strong red fluorescence was seen in the tumors treated with ZnO_2 or Mn-ZnO_2 NPs, reaching as high as 12.0 times and 11.7 times of the saline controls, respectively (Fig. 6d). Negligible fluorescence was detected in the tumors treated with dual ions (Zn^{2+} + Mn^{2+}). These *in vivo* results suggested that Mn-ZnO_2 NPs were able to accumulate in the tumors, locally release dual Zn^{2+}/Mn^{2+} ions and ROS and subsequently cause tumor cell death.

To assure that Mn-ZnO_2 NPs could elicit Mutp53 degradation and activate the ATM-WTp53-Bax signaling under an *in vivo* circumstance, we also assessed the key proteins in the excised tumors by western blotting. Notably, efficient degradation of Mutp53 protein did happen in the tumors treated with ZnO_2 or Mn-ZnO_2 NPs (Fig. 6f and Fig. S19), but no change in Mutp53 mRNA (Fig. S20), implying the post-translational event of Mutp53 degradation by Mn-ZnO_2 NPs. Activation of the ATM-WTp53-Bax signaling by Mn-ZnO_2 NPs took place through the phosphorylation of ATM instead of elevating the overall ATM protein level, *i.e.*, no change in total ATM among all the experimental groups (Fig. 6f and Fig. S19). Compared to the saline controls, Zn^{2+} + Mn^{2+} treatment did not induce any noticeable difference in terms of the phosphorylation

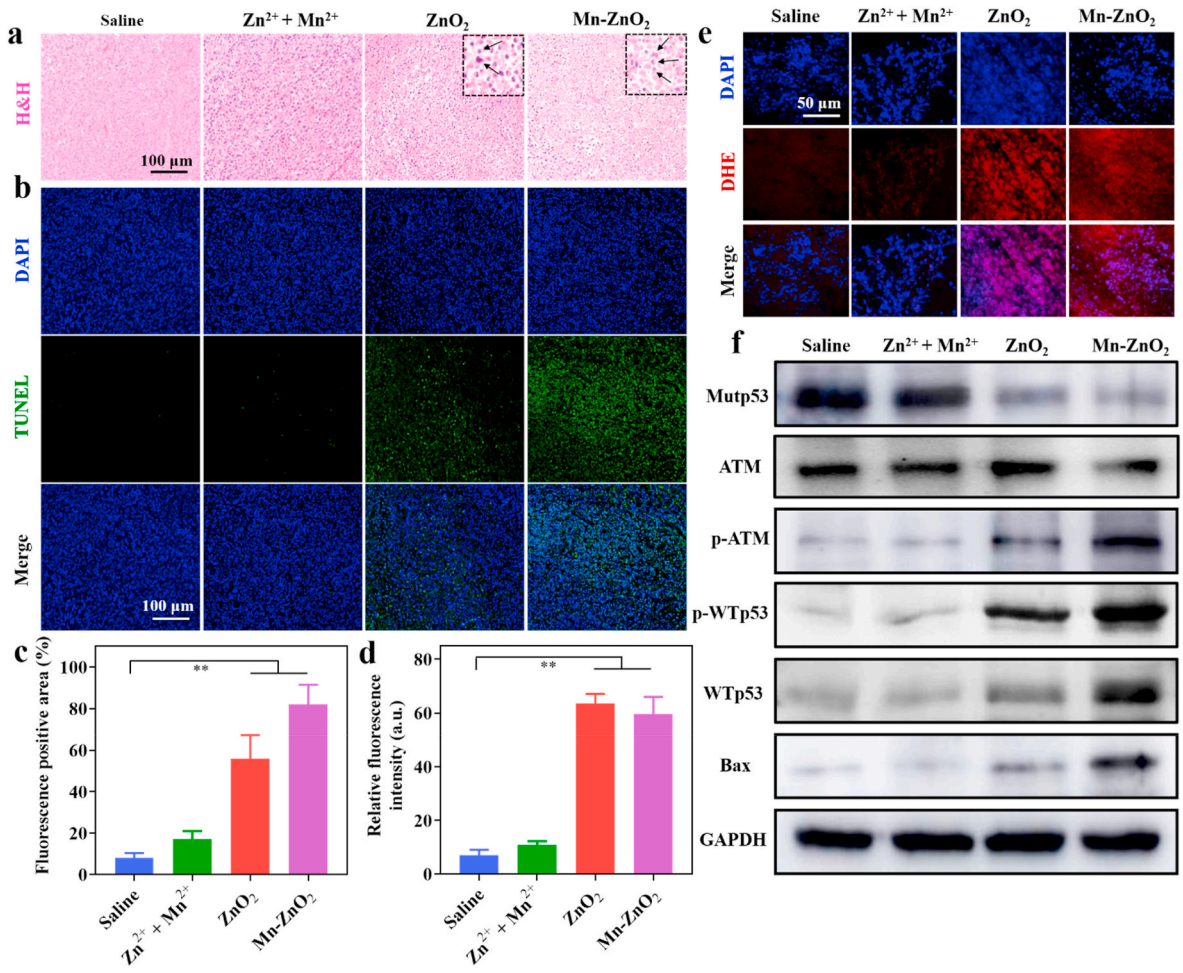

Fig. 6. Histological, histochemical and protein analyses of the tumors treated with Mn-ZnO_2 NPs. (a) H&E-stained cross sections of the resected tumors with different treatments. Arrows of the insets indicate necrotic cells. (b) TUNEL staining (green) of the cross-sections of tumors with different treatments to detect the apoptotic cells. Nuclei were stained with DAPI (blue). (c) Semi-quantification of the TUNEL-positive areas shown in (b). Data are shown as mean ± SD. $^{**}p < 0.01$. (d) Semi-quantification of the DHE fluorescence signal from different groups shown in (e). Fluorescence images ($n \geq 5$ for each group) were analyzed by ImageJ (NIH). Data are shown as mean ± SD. $^{**}p < 0.01$. (e) Fluorescence images of ROS generation within the tumors with different treatments. ROS was stained red with DHE staining. (f) Western blotting of Mutp53, ATM, WT p53, Bax, and GAPDH of the excised tumors with different treatments.

of ATM and WTp53, and the total WTp53 and Bax. The treatment with ZnO_2 NPs on the other hand was able to partially boost the phosphorylation of ATM and WTp53 while enhancing the total WTp53 and Bax level. Interestingly, Mn-ZnO_2 NPs yielded the highest protein level of p-ATM, p-WTp53, WTp53, and Bax (Fig. 6f) and upregulation of both WTp53 and Bax gene (Fig. S20). Collectively, the above results demonstrated the *in vivo* superiority of Mn-ZnO_2 nanoprodrug for enhanced therapy of p53 mutant cancer.

To maximize the use of animals, biosafety of Mn-ZnO_2 NPs was also evaluated along with the therapeutic assessment. First, no significant body weight change was observed under various therapeutic treatments (Fig. S21a). Biochemical analyses of blood collected from the mice showed comparable liver and kidney functions between Mn-ZnO_2 NP-treated and nontreated mice at day 8 and 16 (Figs. S21b–e). Routine blood analysis of Mn-ZnO_2 NP-treated mice for 16 days also confirmed the maintenance of normal range of eleven blood indexes including white blood cell (WBC), red blood cells (RBC), hemoglobin (HGB), hematocrit (HCT), mean corpuscular volume (MCV), mean corpuscular hemoglobin (MCH), mean corpuscular hemoglobin concentration (MCHC), mean platelet volume (MPV), platelets (PLT), red cell distribution width (RDW), and plateletcrit (PCT), suggesting negligible blood toxicity of Mn-ZnO_2 NPs (Fig. S21f-p). Histological analyses of major organs harvested after 16-day treatment with Mn-ZnO_2 NPs showed no signs of tissue damage or inflammatory injury (Fig. S22), confirming negligible toxicity to major organs as well. All above analyses demonstrate that Mn-ZnO_2 nanosystems have good *in vivo* biocompatibility as a promising therapeutic agent for future p53-mutated cancer therapy.

4. Conclusion

In summary, we developed a new concept of carrier-free nanoprodrug (Mn-ZnO_2) to simultaneously deliver dual ions (Mn^{2+} and Zn^{2+}) and ROS to the tumor site without other materials, which would reduce unwanted inflammation and eliminate the concerns on incomplete clearance. Meanwhile, the demonstrated Mn-ZnO_2 nanoprodrug is a T_1-weighted MRI-ready NP with the capabilities of degrading Mutp53, activating WTp53, and generating toxic •OH for selective therapy of p53-mutant tumors. More specifically, due to their pH sensitivity, such Mn-ZnO_2 NPs can completely decompose to Mn^{2+}, Zn^{2+}, and H_2O_2 at a mild acidic microenvironment upon cellular ingestion. Elevated intracellular Zn^{2+} level in conjunction of ROS generation induces Mutp53 degradation *via* the ubiquitination-mediated proteasomal pathway. In parallel, the released Mn^{2+} activates the ATM-WTp53-Bax pathway for the prominent anticancer effect. Consistent with the *in vitro* evidence that Mn-ZnO_2 NPs can elevate the intracellular Zn^{2+}/Mn^{2+} and ROS level, generate cytotoxic •OH through the Fenton-like reaction and

rebalance the Mutp53/WTp53 level, *in vivo* studies further demonstrate that such a nanoprodrug can effectively modulate the p53 level to achieve a high therapeutic efficiency for p53-mutant tumor. Overall, the reported findings provide a simple yet efficient route to synthesize carrier-free nanoprodrug for potential utility in p53-mutant tumor therapy. The synthesis method can be readily extended to other ions-doped metal peroxide nanoparticles for additional ion and ROS delivery. Besides, the strategy of using engineered nanomaterials to address the challenges imposed by Mutp53 degradation and WTp53 upregulation also offer a compelling alternative to p53-targeting drugs for p53-mutant tumor therapy.

Declaration of competing interest

The authors declare no known competing financial interest.

Ethics approval

All animal experiments were carried out in accordance with the guidelines evaluated and approved by the ethics committee of Hebei University of Technology.

CRediT authorship contribution statement

Jinping Wang: Investigation, Methodology, Data curation, Funding acquisition, Writing – original draft. **Chang Qu:** Methodology, Data curation. **Xinyue Shao:** Investigation, Data curation. **Guoqiang Song:** Data curation. **Jingyu Sun:** Data curation. **Donghong Shi:** Methodology. **Ran Jia:** Methodology. **Hailong An:** Supervision, Funding acquisition, Writing – review & editing. **Hongjun Wang:** Conceptualization, Supervision, Funding acquisition, Writing -review & editing.

Acknowledgements

This study was financially supported by the NIAMS award number 1R01AR067859, National Natural Science Foundation of China (82102208, 81830061), Program for Excellent Innovative Talents in Universities of Hebei Province (BJ2021019), and Natural Science Foundation of Hebei Province (H2021202002, H2020202005), the Natural Science Foundation of Tianjin (19JCYBJC28300). The authors would like to thank Dr. Tsengming Chou (Alex) from the Laboratory for Multiscale Imaging at Stevens Institute of Technology for his help in TEM imaging.

Appendix A. Supplementary data

Supplementary data to this article can be found online at https://doi.org/10.1016/j.bioactmat.2022.06.005.

References

[1] B.J. Aubrey, G.L. Kelly, A. Janic, M.J. Herold, A. Strasser, How does p53 induce apoptosis and how does this relate to p53-mediated tumour suppression? Cell Death Differ. 25 (1) (2018) 104–113.
[2] Q. Hao, J. Chen, J. Liao, Y. Huang, Y. Gan, S. Larisch, S.X. Zeng, H. Lu, X. Zhou, p53 induces ARTS to promote mitochondrial apoptosis, Cell Death Dis. 12 (2) (2021) 204.
[3] K.T. Bieging, S.S. Mello, L.D. Attardi, Unravelling mechanisms of p53-mediated tumour suppression, Nat. Rev. Cancer 14 (5) (2014) 359–370.
[4] X. Wang, E.R. Simpson, K.A. Brown, p53: protection against tumor growth beyond effects on cell cycle and apoptosis, Cancer Res. 75 (23) (2015) 5001.
[5] A.J. Patricia, Muller, H. Karen, Vousden, Mutant p53 in cancer: new functions and therapeutic opportunities, Cancer Cell 25 (3) (2014) 304–317.
[6] M.J. Duffy, N.C. Synnott, J. Crown, Mutant p53 as a target for cancer treatment, Eur. J. Cancer 83 (2017) 258–265.
[7] Cancer Genome Atlas Research Network, Nature comprehensive molecular portraits of human breast tumours, Nature 490 (7418) (2012) 61–70.
[8] A.N. Bullock, A.R. Fersht, Rescuing the function of mutant p53, Nat. Rev. Cancer 1 (1) (2001) 68–76.
[9] P.A.J. Muller, K.H. Vousden, p53 mutations in cancer, Nat. Cell Biol. 15 (1) (2013) 2–8.
[10] K.P. Olive, D.A. Tuveson, Z.C. Ruhe, B. Yin, N.A. Willis, R.T. Bronson, D. Crowley, T. Jacks, Mutant p53 gain of function in two mouse models of li-fraumeni syndrome, Cell 119 (6) (2004) 847–860.
[11] Y. Stein, V. Rotter, R. Aloni-Grinstein, Gain-of-function mutant p53: all the roads lead to tumorigenesis, Int. J. Mol. Sci. 20 (24) (2019).
[12] A. Sigal, V. Rotter, Oncogenic mutations of the p53 tumor suppressor: the demons of the guardian of the genome, Cancer Res. 60 (24) (2000) 6788.
[13] G. Liu, T.J. McDonnell, R. Montes de Oca Luna, M. Kapoor, B. Mims, A.K. El-Naggar, G. Lozano, High metastatic potential in mice inheriting a targeted p53 missense mutation, Proc. Natl. Acad. Sci. USA 97 (8) (2000) 4174.
[14] P.A.J. Muller, P.T. Caswell, B. Doyle, M.P. Iwanicki, E.H. Tan, S. Karim, N. Lukashchuk, D.A. Gillespie, R.L. Ludwig, P. Gosselin, A. Cromer, J.S. Brugge, O. J. Sansom, J.C. Norman, K.H. Vousden, Mutant p53 drives invasion by promoting integrin recycling, Cell 139 (7) (2009) 1327–1341.
[15] X. Yue, Y. Zhao, Y. Xu, M. Zheng, Z. Feng, W. Hu, Mutant p53 in cancer: accumulation, gain-of-function, and therapy, J. Mol. Biol. 429 (11) (2017) 1595–1606.
[16] S. Zhang, L. Zhou, B. Hong, A.P.J. van den Heuvel, V.V. Prabhu, N.A. Warfel, C.L. B. Kline, D.T. Dicker, L. Kopelovich, W.S. El-Deiry, Small-molecule NSC59984 restores p53 pathway signaling and antitumor effects against colorectal cancer via p73 activation and degradation of mutant p53, Cancer Res. 75 (18) (2015) 3842.
[17] D. Li, N.D. Marchenko, R. Schulz, V. Fischer, T. Velasco-Hernandez, F. Talos, U. M. Moll, Functional inactivation of endogenous MDM2 and CHIP by HSP90 causes aberrant stabilization of mutant p53 in human cancer cells, Mol. Cancer Res. 9 (5) (2011) 577.
[18] A. Parrales, A. Ranjan, Swathi V. Iyer, S. Padhye, Scott J. Weir, A. Roy, T. Iwakuma, DNAJA1 controls the fate of misfolded mutant p53 through the mevalonate pathway, Nat. Cell Biol. 18 (11) (2016) 1233–1243.
[19] A. Padmanabhan, N. Candelaria, K.-K. Wong, B.C. Nikolai, D.M. Lonard, B. W. O'Malley, J.S. Richards, USP15-dependent lysosomal pathway controls p53-R175H turnover in ovarian cancer cells, Nat. Commun. 9 (1) (2018) 1270.
[20] G. Foggetti, L. Ottaggio, D. Russo, P. Monti, P. Degan, G. Fronza, P. Menichini, Gambogic acid counteracts mutant p53 stability by inducing autophagy, Biochim. Biophys. Acta Mol. Cell Res. 1864 (2) (2017) 382–392.
[21] G. Foggetti, L. Ottaggio, D. Russo, C. Mazzitelli, P. Monti, P. Degan, M. Miele, G. Fronza, P. Menichini, Autophagy induced by SAHA affects mutant P53 degradation and cancer cell survival, Biosci. Rep. 39 (2) (2019), BSR20181345.
[22] L.-S. Lin, J.-F. Wang, J. Song, Y. Liu, G. Zhu, Y. Dai, Z. Shen, R. Tian, J. Song, Z. Wang, W. Tang, G. Yu, Z. Zhou, Z. Yang, T. Huang, G. Niu, H.-H. Yang, Z.-Y. Chen, X. Chen, Cooperation of endogenous and exogenous reactive oxygen species induced by zinc peroxide nanoparticles to enhance oxidative stress-based cancer therapy, Theranostics 9 (24) (2019) 7200–7209.
[23] J. Qian, W. Zhang, P. Wei, G. Yao, T. Yi, H. Zhang, H. Ding, X. Huang, M. Wang, Y. Song, S. Zhong, L. Yang, J. Gao, Z. Zhou, L.-p. Wen, Y. Zhang, Enhancing chemotherapy of p53-mutated cancer through ubiquitination-dependent proteasomal degradation of mutant p53 proteins by engineered ZnFe-4 nanoparticles, Adv. Funct. Mater. 30 (40) (2020), 2001994.
[24] A.M. Tidball, M.R. Bryan, M.A. Uhouse, K.K. Kumar, A.A. Aboud, J.E. Feist, K. C. Ess, M.D. Neely, M. Aschner, A.B. Bowman, A novel manganese-dependent ATM-p53 signaling pathway is selectively impaired in patient-based neuroprogenitor and murine striatal models of Huntington's disease, Hum. Mol. Genet. 24 (7) (2015) 1929–1944.
[25] K.J. Horning, S.W. Caito, K.G. Tipps, A.B. Bowman, M. Aschner, Manganese is essential for neuronal health, Annu. Rev. Nutr. 35 (1) (2015) 71–108.
[26] J.-M. Lai, J.T. Chang, C.-L. Wen, S.-L. Hsu, Emodin induces a reactive oxygen species-dependent and ATM-p53-Bax mediated cytotoxicity in lung cancer cells, Eur. J. Pharmacol. 623 (1) (2009) 1–9.
[27] Z. Guo, S. Kozlov, F. Lavin Martin, D. Person Maria, T. Paull Tanya, ATM activation by oxidative stress, Science 330 (6003) (2010) 517–521.
[28] M. Chang, M. Wang, M. Wang, M. Shu, B. Ding, C. Li, M. Pang, S. Cui, Z. Hou, J. Lin, A multifunctional cascade bioreactor based on hollow-structured Cu_2MoS_4 for synergetic cancer chemo-dynamic therapy/starvation therapy/phototherapy/immunotherapy with remarkably enhanced efficacy, Adv. Mater. 31 (51) (2019), 1905271.
[29] Y. Liu, M. Zhang, W. Bu, Bioactive nanomaterials for ion-interference therapy, View 1 (2) (2020) e18.
[30] R.B. Greenwald, Y.H. Choe, J. McGuire, C.D. Conover, Effective drug delivery by PEGylated drug conjugates, Adv. Drug Deliv. Rev. 55 (2) (2003) 217–250.
[31] S. Nowag, C. Frangville, G. Multhaup, J.D. Marty, C. Mingotaud, R. Haag, Biocompatible, hyperbranched nanocarriers for the transport and release of copper ions, J. Mater. Chem. B 2 (25) (2014) 3915–3918.
[32] M.-K. Zhang, J.-J. Ye, C.-X. Li, Y. Xia, Z.-Y. Wang, J. Feng, X.-Z. Zhang, Cytomembrane-mediated transport of metal ions with biological specificity, Adv. Sci. 6 (17) (2019), 1900835.
[33] Ş.Ş. Türkyılmaz, N. Güy, M. Özacar, Photocatalytic efficiencies of Ni, Mn, Fe and Ag doped ZnO nanostructures synthesized by hydrothermal method: the synergistic/antagonistic effect between ZnO and metals, J. Photochem. Photobiol., A 341 (2017) 39–50.
[34] Y. Zhang, X. Huang, L. Wang, C. Cao, H. Zhang, P. Wei, H. Ding, Y. Song, Z. Chen, J. Qian, S. Zhong, Z. Liu, M. Wang, W. Zhang, W. Jiang, J. Zeng, G. Yao, L. Wen, Glutathionylation-dependent proteasomal degradation of wide-spectrum mutant p53 proteins by engineered zeolitic imidazolate framework-8, Biomaterials 271 (2021), 120720.

[35] Y. Zhu, W. Zhao, H. Chen, J. Shi, A simple one-pot self-assembly route to nanoporous and monodispersed Fe_3O_4 particles with oriented attachment structure and magnetic property, J. Phys. Chem. C 111 (14) (2007) 5281–5285.
[36] Y. Borodko, S.E. Habas, M. Koebel, P. Yang, H. Frei, G.A. Somorjai, Probing the interaction of poly(vinylpyrrolidone) with platinum nanocrystals by UV−Raman and FTIR, J. Phys. Chem. B 110 (46) (2006) 23052–23059.
[37] L.-S. Lin, X. Yang, Z. Zhou, Z. Yang, O. Jacobson, Y. Liu, A. Yang, G. Niu, J. Song, H.-H. Yang, X. Chen, Yolk–shell nanostructure: an ideal architecture to achieve harmonious integration of magnetic-plasmonic hybrid theranostic platform, Adv. Mater. 29 (21) (2017), 1606681.
[38] W. Chen, Y.H. Lu, M. Wang, L. Kroner, H. Paul, H.J. Fecht, J. Bednarcik, K. Stahl, Z. L. Zhang, U. Wiedwald, U. Kaiser, P. Ziemann, T. Kikegawa, C.D. Wu, J.Z. Jiang, Synthesis, thermal stability and properties of ZnO_2 nanoparticles, J. Phys. Chem. C 113 (4) (2009) 1320–1324.
[39] S. Cheng, D. Yan, J.T. Chen, R.F. Zhuo, J.J. Feng, H.J. Li, H.T. Feng, P.X. Yan, Soft-template synthesis and characterization of ZnO_2 and ZnO hollow spheres, J. Phys. Chem. C 113 (31) (2009) 13630–13635.
[40] S. Shen, M. Mamat, S. Zhang, J. Cao, Z.D. Hood, L. Figueroa-Cosme, Y. Xia, Synthesis of CaO_2 nanocrystals and their spherical aggregates with uniform sizes for use as a biodegradable bacteriostatic agent, Small 15 (36) (2019), 1902118.
[41] M.-V. Clement, L.H. Long, J. Ramalingam, B. Halliwell, The cytotoxicity of dopamine may be an artefact of cell culture, J. Neurochem. 81 (3) (2002) 414–421.
[42] H. Meng, Y. Li, M. Faust, S. Konst, B.P. Lee, Hydrogen peroxide generation and biocompatibility of hydrogel-bound mussel adhesive moiety, Acta Biomater. 17 (2015) 160–169.
[43] L. Feng, Z. Dong, D. Tao, Y. Zhang, Z. Liu, The acidic tumor microenvironment: a target for smart cancer nano-theranostics, Natl. Sci. Rev. 5 (2) (2018) 269–286.
[44] H.B. Na, J.H. Lee, K. An, Y.I. Park, M. Park, I.S. Lee, D.-H. Nam, S.T. Kim, S.-H. Kim, S.-W. Kim, K.-H. Lim, K.-S. Kim, S.-O. Kim, T. Hyeon, Development of a T1 contrast agent for magnetic resonance imaging using MnO nanoparticles, Angew. Chem., Int. Ed. Engl. 46 (28) (2007) 5397–5401.
[45] L.-S. Lin, J. Song, L. Song, K. Ke, Y. Liu, Z. Zhou, Z. Shen, J. Li, Z. Yang, W. Tang, G. Niu, H.-H. Yang, X. Chen, Simultaneous fenton-like ion delivery and glutathione depletion by MnO_2-based nanoagent to enhance chemodynamic therapy, Angew. Chem., Int. Ed. Engl. 57 (18) (2018) 4902–4906.
[46] T. He, X. Qin, C. Jiang, D. Jiang, S. Lei, J. Lin, W.-G. Zhu, J. Qu, P. Huang, Tumor pH-responsive metastable-phase manganese sulfide nanotheranostics for traceable hydrogen sulfide gas therapy primed chemodynamic therapy, Theranostics 10 (6) (2020) 2453–2462.
[47] L.-H. Fu, Y.-R. Hu, C. Qi, T. He, S. Jiang, C. Jiang, J. He, J. Qu, J. Lin, P. Huang, Biodegradable manganese-doped calcium phosphate nanotheranostics for traceable cascade reaction-enhanced anti-tumor therapy, ACS Nano 13 (12) (2019) 13985–13994.
[48] Z. Tang, Y. Liu, M. He, W. Bu, Chemodynamic therapy: tumour microenvironment-mediated fenton and fenton-like reactions, Angew. Chem., Int. Ed. Engl. 58 (4) (2019) 946–956.
[49] L. Hui, Y. Zheng, Y. Yan, J. Bargonetti, D.A. Foster, Mutant p53 in MDA-MB-231 breast cancer cells is stabilized by elevated phospholipase D activity and contributes to survival signals generated by phospholipase D, Oncogene 25 (55) (2006) 7305–7310.
[50] J. Noh, B. Kwon, E. Han, M. Park, W. Yang, W. Cho, W. Yoo, G. Khang, D. Lee, Amplification of oxidative stress by a dual stimuli-responsive hybrid drug enhances cancer cell death, Nat. Commun. 6 (1) (2015) 6907.
[51] L.-S. Lin, T. Huang, J. Song, X.-Y. Ou, Z. Wang, H. Deng, R. Tian, Y. Liu, J.-F. Wang, Y. Liu, G. Yu, Z. Zhou, S. Wang, G. Niu, H.-H. Yang, X. Chen, Synthesis of copper peroxide nanodots for H_2O_2 self-supplying chemodynamic therapy, J. Am. Chem. Soc. 141 (25) (2019) 9937–9945.
[52] Z. Wang, Y. Zhang, E. Ju, Z. Liu, F. Cao, Z. Chen, J. Ren, X. Qu, Biomimetic nanoflowers by self-assembly of nanozymes to induce intracellular oxidative damage against hypoxic tumors, Nat. Commun. 9 (1) (2018) 3334.
[53] V. Kolenko, E. Teper, A. Kutikov, R. Uzzo, Zinc and zinc transporters in prostate carcinogenesis, Nat. Rev. Urol. 10 (4) (2013) 219–226.
[54] R.B. Franklin, L.C. Costello, Zinc as an anti-tumor agent in prostate cancer and in other cancers, Arch. Biochem. Biophys. 463 (2) (2007) 211–217.
[55] D. Kleiner, The effect of Zn^{2+} ions on mitochondrial electron transport, Arch. Biochem. Biophys. 165 (1) (1974) 121–125.
[56] K.E. Dineley, L.L. Richards, T.V. Votyakova, I.J. Reynolds, Zinc causes loss of membrane potential and elevates reactive oxygen species in rat brain mitochondria, Mitochondrion 5 (1) (2005) 55–65.
[57] R. Bresolí-Obach, L. Busto-Moner, C. Muller, M. Reina, S. Nonell, NanoDCFH-DA: a silica-based nanostructured fluorogenic probe for the detection of reactive oxygen species, Photochem. Photobiol. 94 (6) (2018) 1143–1150.
[58] W.-Y. Shen, C.-P. Jia, A.-N. Mo, H. Liang, Z.-F. Chen, Chemodynamic therapy agents Cu(II) complexes of quinoline derivatives induced ER stress and mitochondria-mediated apoptosis in SK-OV-3 cells, Eur. J. Med. Chem. 223 (2021), 113636.
[59] N. Guo, Z. Peng, MG132, a proteasome inhibitor, induces apoptosis in tumor cells, Asia-pac, J. Clin. Oncol. 9 (1) (2013) 6–11.
[60] F.A. Mallette, S. Richard, K48-linked ubiquitination and protein degradation regulate 53BP1 recruitment at DNA damage sites, Cell Res. 22 (8) (2012) 1221–1223.
[61] S.V. Kozlov, A.J. Waardenberg, K. Engholm-Keller, J.W. Arthur, M.E. Graham, M. Lavin, Reactive oxygen species (ROS)-activated ATM-dependent phosphorylation of cytoplasmic substrates identified by large-scale phosphoproteomics screen, Mol. Cell. Proteomics 15 (3) (2016) 1032–1047.
[62] C.J. Bakkenist, M.B. Kastan, DNA damage activates ATM through intermolecular autophosphorylation and dimer dissociation, Nature 421 (6922) (2003) 499–506.
[63] E. Canman Christine, D.-S. Lim, A. Cimprich Karlene, Y. Taya, K. Tamai, K. Sakaguchi, E. Appella, B. Kastan Michael, D. Siliciano Janet, Activation of the atm kinase by ionizing radiation and phosphorylation of p53, Science 281 (5383) (1998) 1677–1679.
[64] H. Shen, L. Liu, Y. Yang, W. Xun, K. Wei, G. Zeng, Betulinic acid inhibits cell proliferation in human oral squamous cell carcinoma via modulating ROS-regulated p53 signaling, Oncol. Res. 25 (7) (2017) 1141–1152.
[65] S.K. Hobbs, W.L. Monsky, F. Yuan, W.G. Roberts, L. Griffith, V.P. Torchilin, R. K. Jain, Regulation of transport pathways in tumor vessels: role of tumor type and microenvironment, Proc. Natl. Acad. Sci. USA 95 (8) (1998) 4607.
[66] Y. Han, Z. Chen, H. Zhao, Z. Zha, W. Ke, Y. Wang, Z. Ge, Oxygen-independent combined photothermal/photodynamic therapy delivered by tumor acidity-responsive polymeric micelles, J. Contr. Release 284 (2018) 15–25.